

Sterically Invariant Carborane-Based Ligands for the Morphological and Electronic Control of Metal-Organic Chalcogenolate Assemblies

Harrison A. Mills^a, Christopher G. Jones^{a,b}, Kierstyn P. Anderson^a, Austin D. Ready^a, Peter I. Djurovich^c, Saeed I. Khan^a, J. Nathan Hohman^{*d}, Hosea M. Nelson^{*a,b}, Alexander M. Spokoyny^{*a,e}

^aDepartment of Chemistry and Biochemistry, University of California, Los Angeles, Los Angeles, California 90095, United States

^bDivision of Chemistry and Chemical Engineering, California Institute of Technology, Pasadena, California 91125, United States

^cDepartment of Chemistry, University of Southern California, Los Angeles, California 90089, United States

^dInstitute of Materials Science and the Department of Chemistry, University of Connecticut, Storrs, Connecticut 06269, United States

^eCalifornia NanoSystems Institute (CNSI), University of California, Los Angeles, Los Angeles, California 90095, United States

SUPPLEMENTARY INFORMATION

*Emails: spokoyny@chem.ucla.edu; hosea@chem.ucla.edu; james.hohman@uconn.edu.

Table of Contents

1. General Considerations.....	S3
2. Instrumentation.....	S3
3. Synthesis of Chalcogenols	S5
4. Synthesis of MOCHAs (A-D).....	S9
5. Supplementary Characterization and Data of A.....	S11
a. Additional Electron Microscopy Images.....	S11
b. Powder X-ray Diffraction Pattern.....	S13
c. Infrared Spectroscopy.....	S14
d. Thermogravimetric Analysis.....	S14
e. X-ray Photoelectron Spectroscopy.....	S15
f. Photophysical Measurements.....	S17
g. DFT Calculations.....	S19
6. Supplementary Characterization and Data of B.....	S21
a. Additional Electron Microscopy Images.....	S21
b. Powder X-ray Diffraction Pattern.....	S23
c. Infrared Spectroscopy.....	S23
d. Thermogravimetric Analysis.....	S24
e. X-ray Photoelectron Spectroscopy.....	S25
f. Photophysical Measurements.....	S27
g. Attempted MicroED.....	S28
7. Supplementary Characterization and Data of C.....	S29
a. Additional Electron Microscopy Images.....	S29
b. Powder X-ray Diffraction Pattern.....	S31
c. Infrared Spectroscopy.....	S31
d. Thermogravimetric Analysis.....	S32
e. X-ray Photoelectron Spectroscopy.....	S33
f. Photophysical Measurements.....	S35
g. Attempted MicroED.....	S37
8. Supplementary Characterization and Data of D.....	S38
a. Additional Electron Microscopy Images.....	S38
b. Powder X-ray Diffraction Pattern.....	S40
c. Infrared Spectroscopy.....	S40
d. Thermogravimetric Analysis.....	S41
e. X-ray Photoelectron Spectroscopy.....	S42
f. Photophysical Measurements.....	S44
9. Further Analysis of Literature Copper Selenide Clusters.....	S46
10. ^1H and ^{11}B NMR Experiments of Dissolved Materials A-D in CD_2Cl_2	S48
11. Study and Comparison of Literature PXRD Patterns with Varying Carborane Isomers and Chalcogens.....	S51
12. Qualitative Assessment of Emission Properties in Various Solvents and Media.....	S52
13. References.....	S54

1. General Considerations

Ortho-C₂B₁₀H₁₂ (Boron Specialties) was sublimed prior to use. *Meta*-C₂B₁₀H₁₂ (Katchem or Alfa Aesar) was used as is. Anhydrous dichloromethane was obtained from a Grubbs column with activated alumina and copper catalyst. Se₂Cl₂ used in the synthesis of **9-HSe-mCB** and **9-HSe-oCB** was prepared according to the procedure found in reference 1 and subsequently stored in a PTFE-capped vial at -15 °C. *Iso*-propanol (200 proof) was purchased from Fisher Sci., Certified ACS quality. *Iso*-propanol used in the synthesis of materials **A-D** was dried by refluxing 100 mL of *iso*-propanol over 5g of elemental magnesium chips with vigorous stirring. After refluxing overnight, the anhydrous *iso*-propanol was distilled under an atmosphere of N₂ into a 100 mL Schlenk tube containing activated 3Å molecular sieves. The Schlenk tube was sealed with a Teflon stopper and stored in ambient conditions. Cu(OAc) of 97% purity was purchased from Strem Chemical Inc. and stored in an N₂-filled glovebox at -30 °C. All other reagents were purchased from commercial vendors and used as is. All synthesized chalcogenols were stored in an N₂-filled glovebox at -30 °C for long term storage. Unless otherwise stated, all reactions were performed under an inert atmosphere of N₂ either in a glovebox or using a Schlenk line, and all manipulations were performed under ambient laboratory air, exposed to ambient light.

2. Instrumentation

¹H, ¹¹B, and ⁷⁷Se NMR spectra were recorded on either a Bruker DRX500 or Bruker AVIII HD 400 spectrometers in ambient conditions at room temperature. MestReNova v6.0.2-5475 software was used to process the FID data and visualize the spectra. ¹H NMR spectra were referenced to residual solvent resonances in deuterated solvents (note: due to high humidity H₂O resonances are often present) and are reported relative to tetramethylsilane (δ = 0 ppm). ¹¹B NMR spectra were referenced externally to Et₂O•BF₃ (δ = 0 ppm). ⁷⁷Se NMR spectra were referenced externally to diphenyldiselenide (δ = 463.15 ppm). Exponential apodization (5-30 Hz) was applied through MestReNova to ⁷⁷Se spectra in order to enhance the signal to noise ratio.

Elemental analysis of materials **A-D** was performed by Atlantic Microlabs.

Transmission electron microscopy (TEM) was carried out using either an FEI T20 iCorr cryo TEM operated at 200 kV or an FEI T12 TEM operated at 120 kV. TEM samples were prepared by adding 5-10 μ L of a colloidal suspension of nanoparticles in *iso*-propanol to a copper grid (200 mesh, Formvar/Carbon or Carbon Film only, Ted Pella, Redding, CA).

Samples prepared for TEM were additionally used for microcrystal electron diffraction (MicroED) experiments. The prepared TEM grid was loaded in a Gatan 626 single-tilt cryo holder and cooled with liquid nitrogen. Screening and data collection were performed using a Thermo-Fisher F200C transmission electron microscope operating at 200 kV corresponding to a wavelength of 0.0251 Å. Electron diffraction data were collected using a Thermo-Fischer Ceta-D CMOS 4k \times 4k camera. The screening of crystals was done in low-dose mode and diffraction was identified through condensing of the electron beam. After the selection of a crystal on the grid, the crystal was centered, the eucentric height adjusted by tilting the crystal through the desired rotation range, and the selected area aperture and beam stop were inserted (reference 2). Images were collected in a movie format as crystals were continuously rotated in the electron beam (reference 3). Typical

data collection was performed using a constant tilt rate of 0.3°/s between the minimum and maximum tilt ranges of -72° to +72°, respectively. During continuous rotation, the camera integrated frames continuously at a rate of 3 seconds per frame. The dose rate was calibrated to <0.03 e⁻/Å² s. Crystals selected for data collection were isolated by a selected area aperture to reduce the background noise contributions and calibrated to eucentric height to stay in the aperture over the entire tilt range. The electron diffraction data were processed using the XDS suite of programs (reference 4). To achieve a sufficient number of reflections datasets from five different crystals were merged and scaled with XSCALE. The structure was solved *ab initio* using direct methods in SHELXT (reference 5) using ShelXle (reference 6). Structure refinement was performed using electron scattering factors reported by Peng (reference 7). Thermal parameters were refined anisotropically for all non-hydrogen atoms.

Scanning electron microscopy (SEM) was carried out using a ZEISS SUPRAU 40VP Field Emission Scanning Electron Microscope operating at 30 kV. SEM samples were prepared by adding several drops of a colloidal suspension of nanocrystals in *iso*-propanol to a square-cut chip of silicon wafer.

X-ray photoelectron spectroscopy (XPS) measurements were performed on an AXIS Ultra DLD instrument (Kratos Analytical Inc.). Spectra were obtained using a monochromatic Al K α X-ray source (Filament current: 1.8 A) with a 10 mA emission current and an anode voltage of 15 kV. Survey spectra were conducted with a pass energy of 160 eV, 1 eV step size, and 100 ms dwell time. High-resolution spectra were conducted with a pass energy of 20 eV, 1 eV step size, and 600 ms dwell time. All spectra were measured with automatic charge neutralization and referenced to the adventitious carbon 1s signal at 284.6 eV. XPS data was further processed and peak fitted using CasaXPS Version 2.3.24PR1.0 (reference 8).

Infrared absorption spectra (FTIR) were obtained using a PerkinElmer Spectrum One spectrometer equipped with a universal ATR assembly. Samples were deposited as dry powders.

Thermogravimetric analysis (TGA) was carried out on a PerkinElmer Pyris Diamond TG/DTA under a constant flow of argon gas (200 mL/min). Samples were heated in alumina oxide trays from 25 °C to 500 °C at a rate of 20 °C/min.

Powder X-ray diffraction (PXRD) was conducted using a Panalytical X'Pert Pro X-ray Powder Diffractometer. Samples were deposited as dry powders onto a zero-background sample holder as a level pellet. Samples were diffracted from 5 to 65 2θ with a step size of 0.016°.

UV-Vis absorption measurements were taken using an Ocean Optics Flame Miniature Spectrometer detector and Ocean Optics DH-2000 UV-Vis-NIR source. All samples were suspended in *iso*-propanol and measurements were taken in a 1 cm quartz cuvette.

Fluorescence emission scans were performed using a Horiba Instruments PTI QuantaMaster Series fluorometer equipped with a PMT detector operated under ambient conditions. Dilute suspensions of microcrystals were prepared in *iso*-propanol and measurements were taken in a 1 cm quartz cuvette.

Quantum yield measurements were carried out using a Hamamatsu C9920 system equipped with a xenon lamp, calibrated integrating sphere, and model C10027 photonic multichannel analyzer (PMA). Samples were deposited as dry powders on quartz plates and excited at 290 nm.

Photoluminescence lifetimes were measured by time-correlated single-photon counting using an IBH Fluorocube instrument equipped with an LED excitation source. Samples were deposited as dry powders on quartz plates and were excited at 372 nm and observed at 550 nm.

3. Synthesis of Chalcogenols

Synthesis of 9-SeH-mCB (A')

Synthetic procedures adapted from reference 9. *Meta*-C₂B₁₀H₁₂ (1.44 g, 10 mmol) and AlCl₃ (1.33 g, 10 mmol, 1 eq) were added to an oven-dried Schlenk flask equipped with a stir bar and rubber septum and evacuated/backfilled with N₂ three times. Anhydrous CH₂Cl₂ (25 ml), collected from a Grubb's column, was added to the Schlenk flask *via* cannula and the solids were allowed to dissolve. Subsequently, Se₂Cl₂ (0.42 mL, 5 mmol, 0.5 eq) was added dropwise to the stirring suspension *via* syringe, forming a dark red solution that was allowed to stir overnight at room temperature. Upon completion of the reaction, determined by TLC, the reaction was carefully quenched by the addition of distilled H₂O (15 mL), yielding a dark yellow, cloudy suspension. The yellow organic layer was separated from the aqueous layer and the aqueous layer was extracted with CH₂Cl₂ (3 x 15 mL). The organic layers were combined and dried with Na₂SO₄, resulting in a clear yellow/orange solution. The solution was then decanted from the Na₂SO₄ and volatiles were removed under reduced pressure to yield the *meta*-carboranyl diselenide. The diselenide was then dissolved in a minimal amount of absolute EtOH (30-50 mL), resulting in a red-orange solution with some solids still suspended (sonication may be required). While stirring the solution of the diselenide, an excess of NaBH₄ (0.80 g) was carefully added over the course of several minutes. During the course of the addition, some heat and gas were generated, with the consumption of the diselenide indicated by the reaction mixture turning cloudy and colorless. The reduction was stirred for an additional 15 minutes before the dropwise addition of aqueous HCl (~2M, 10-20 mL) to quench any residual NaBH₄ and protonate the selenolate intermediate. Once no more gas was evolved upon addition of HCl, distilled H₂O (200 mL) was added resulting in a foamy, pale yellow suspension. The product was then extracted from the aqueous solution with CH₂Cl₂ (4 x 30 mL) and the collected organic layers were dried over Na₂SO₄. The dried organic layers were decanted away from the Na₂SO₄ and all volatiles were removed under reduced pressure, leaving the crude product as a pale-yellow solid. The crude product was further purified *via* vacuum sublimation at 90 °C, affording the product as a white, crystalline solid in 58% yield with a mild odor.

Yield: 1.3 g (58%), white, odorous solid

All characterization matches literature data, and representative ¹H and ¹¹B NMR spectra recorded in CDCl₃ have been provided below:

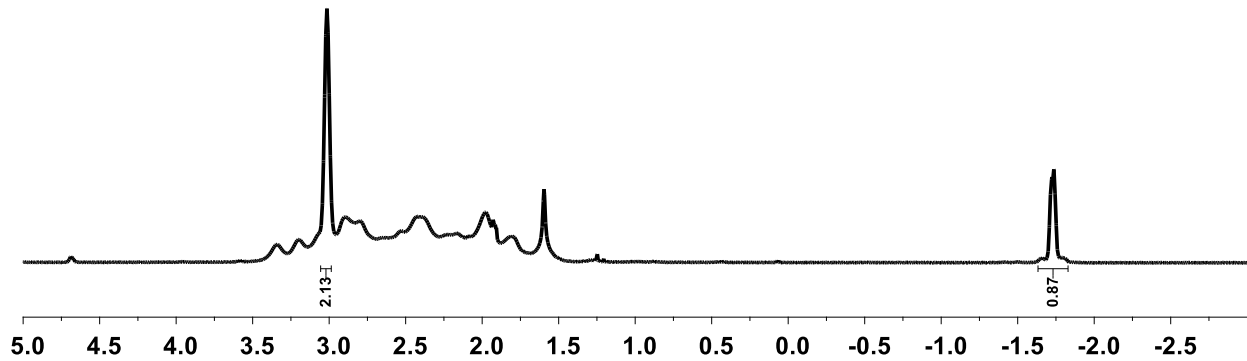


Figure S1: ¹H NMR spectrum of 9-SeH-mCB (A')

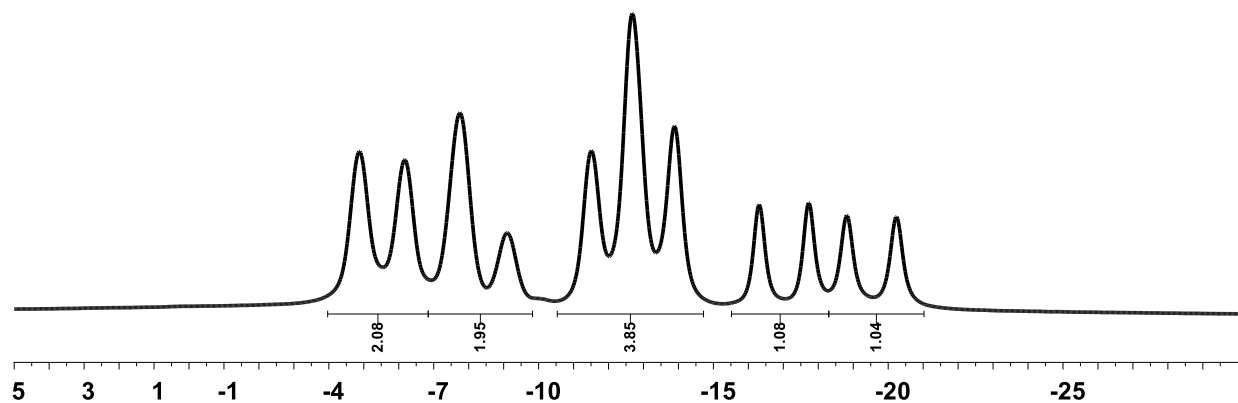


Figure S2: ¹¹B NMR spectrum of 9-SeH-mCB (A')

Synthesis of 9-SeH-oCB (B')

9-HSe-oCB was prepared in an analogous manner as 9-HSe-mCB, where *ortho*-C₂B₁₀H₁₂ was used instead of *meta*-C₂B₁₀H₁₂.

Yield: 720 mg (31%), white, odorous solid

All characterization matches literature data, and representative ¹H and ¹¹B NMR spectra recorded in CDCl₃ have been provided below:

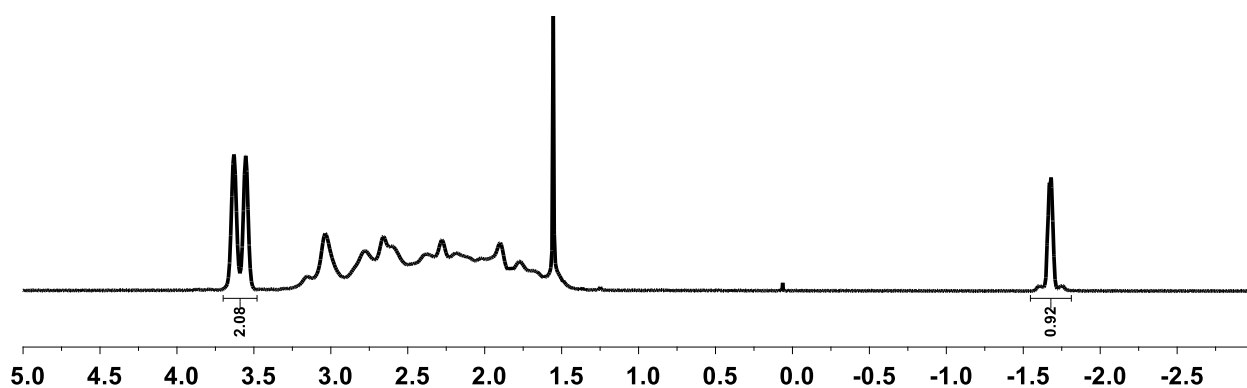


Figure S3: ^1H NMR spectrum of 9-SeH-oCB (**B'**)

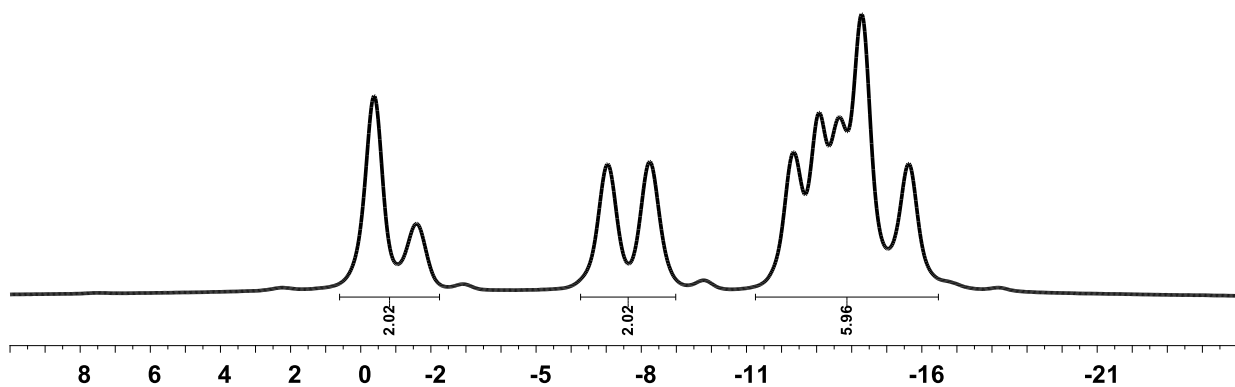


Figure S4: ^{11}B NMR spectrum of 9-SeH-oCB (**B'**)

Synthesis of 9-SH-mCB (**C'**)

Synthetic procedures adapted from references 10 and 11. *Meta*-C₂B₁₀H₁₂ (1.44 g, 10 mmol) and AlCl₃ (1.33 g, 10 mmol, 1 eq) were added to an oven-dried Schlenk flask equipped with a stir bar and rubber septum and evacuated/backfilled with N₂ three times. Anhydrous CH₂Cl₂ (25 ml), collected from a Grubb's column, was added to the Schlenk flask *via* cannula and the solids were allowed to dissolved. Subsequently, S₂Cl₂ (0.42 mL, 5 mmol, 0.5 eq) in 2 mL of anhydrous CH₂Cl₂, was added dropwise to the stirring suspension *via* syringe, forming a red solution that was allowed to stir overnight at room temperature. Upon completion of the reaction, determined by TLC, the reaction was carefully quenched by the addition of distilled H₂O (15 mL), yielding a dark yellow, cloudy suspension. The yellow organic layer was separated from the aqueous layer and the aqueous layer was extracted with CH₂Cl₂ (3 x 15 mL). The organic layers were combined and dried with Na₂SO₄, resulting in a clear yellow/orange solution. The solution was then decanted from the Na₂SO₄ and volatiles were removed under reduced pressure to yield the *meta*-carboranyl disulfide. The disulfide was then dissolved in a minimal amount of absolute EtOH (30-50 mL), resulting in a yellow solution (sonication may be required). While stirring the solution of the disulfide, 1-2 chips of NaOH and excess of NaBH₄ (0.60 g) was carefully added over the course of several minutes. After completing the addition of NaOH and NaBH₄, the flask was capped with a septum and bleed needle before heating to 50 °C for 1 hour. After stirring for 1 hour, the reduction was allowed to cool to room temperature before the dropwise addition of aqueous HCl (~2M, 10-20 mL) to quench any residual NaBH₄ and protonate the thiolate intermediate. Once no more gas was evolved upon addition of HCl, distilled H₂O (200 mL) was added resulting in a foamy, pale yellow suspension. The product was then extracted from the aqueous solution with CH₂Cl₂ (4 x 30 mL) and the collected organic layers were dried over Na₂SO₄. The dried organic layers were decanted away from the Na₂SO₄ and all volatiles were removed under reduced pressure, leaving the crude product as a pale-yellow solid. The crude product was further purified *via* vacuum sublimation at 90 °C, affording the product as a white, crystalline solid in 78% yield with a mild odor.

Yield: 1.4 g (78%), white, odorous solid

All characterization matches literature data, and representative ^1H and ^{11}B NMR spectra recorded in CDCl_3 have been provided below:

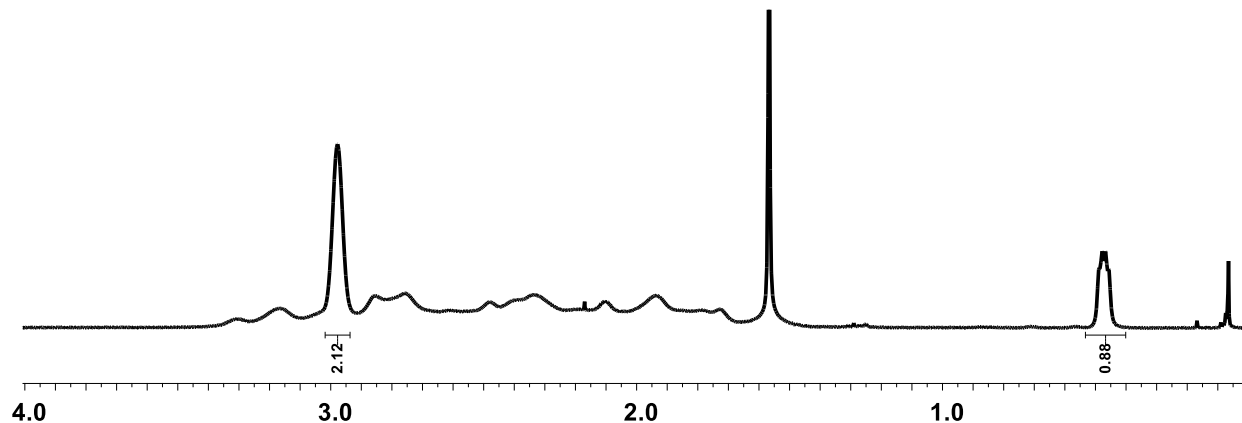


Figure S5: ^1H NMR spectrum of 9-SH-mCB (**C'**)

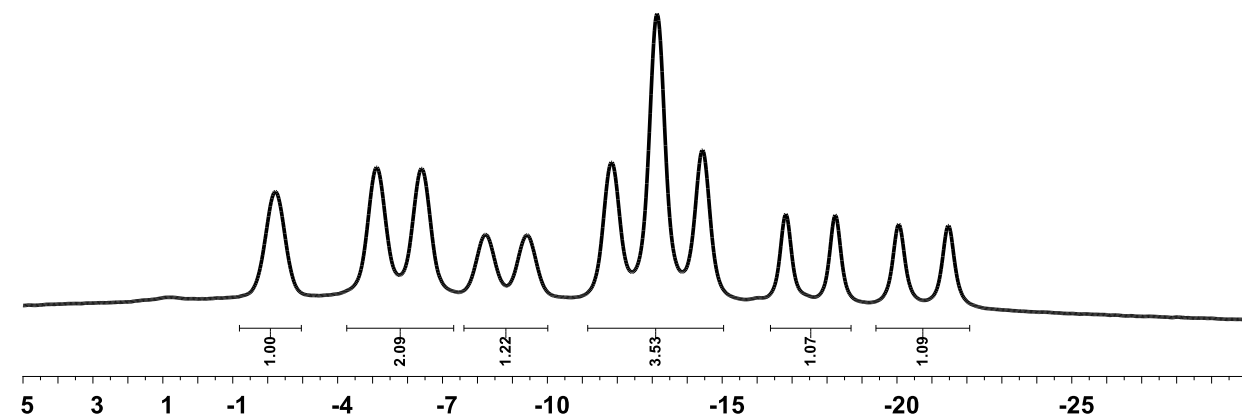


Figure S6: ^{11}B NMR spectrum of 9-SH-mCB (**C'**)

Synthesis of 9-SH-oCB (D')

9-SH-oCB was prepared in an analogous manner as 9-SH-mCB, where *ortho*- $\text{C}_2\text{B}_{10}\text{H}_{12}$ was used instead of *meta*- $\text{C}_2\text{B}_{10}\text{H}_{12}$ and with minor alterations to the reduction procedure. Instead of heating for 1 hour equipped with a bleed needle, the reduction was instead left heating at 50 °C overnight under positive nitrogen pressure. All workup procedures were identical.

Yield: 700 mg (40%), white, odorous solid

All characterization matches literature data, and representative ^1H and ^{11}B NMR spectra recorded in CDCl_3 have been provided below:

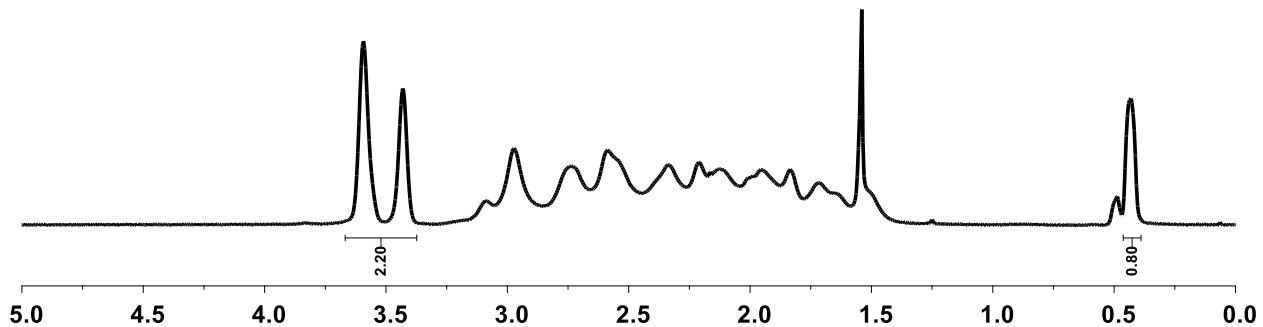


Figure S7: ^1H NMR spectrum of 9-SH-oCB (**D'**)

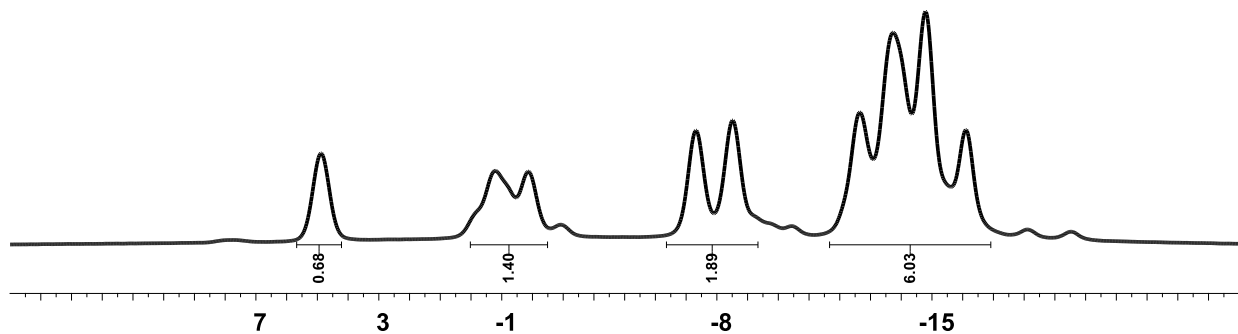


Figure S8: ^{11}B NMR spectrum of 9-SH-oCB (**D'**)

4. Synthesis of MOCHAs (A-D)

General Procedures

An oven-dried 4 mL dram vial equipped with a stir bar and PTFE septa cap was transferred into a N_2 -filled glovebox. In the glovebox, chalcogenol (0.11 mmol; 1.1 eq) and anhydrous copper(I) acetate (12 mg, 0.1 mmol; 1 eq) were subsequently added to the dram vial and sealed with the PTFE cap. The vial was then transferred out of the glove box and anhydrous *iso*-propanol (1 mL, see SI sec. 1 for drying and storage procedures) was quickly added *via* syringe and the resulting suspension was immediately stirred at \sim 700 rpm. The reaction vial was then covered to limit exposure to light and then left to stir for 24 hours.

After stirring for 24 hours, the reaction appeared as milky white, off-white, or pale-yellow suspension. The suspension mixture was then transferred to a pre-weighed screw-capped tube suitable for centrifugation. Additional *iso*-propanol (non-anhydrous) was added to the reaction vial to maximize transfer of product to the screw-capped tube. The suspension was then centrifuged at 2900xg until all material was pelleted at the bottom of the tube (10 minutes). Once pelleted, the supernatant (*iso*-propanol, excess chalcogenol) was decanted from the tube and additional *iso*-propanol (2 mL, non-anhydrous) was added. The screw-capped tube was then vortexed to resuspend all powder before centrifuging once more, and the supernatant decanted. The above

process was repeated once more before drying the pellet on a high-vacuum Schlenk line while in the screw-capped tube to remove all volatiles. After drying, materials **A-D** were afforded as free-flowing powders of varying fluffiness.

Yields:

Cu-[9-Se-mCB] (**A**), off-white/pale-yellow powder: 22 mg, 76%

Elemental Analysis: Calculated for CuSeC₂B₁₀H₁₁: C, 8.41; H, 3.88; found: C, 8.87; H, 3.78 (average of two duplicate runs)

Cu-[9-Se-oCB] (**B**), off-white/pale-yellow powder: 19 mg, 65%

Elemental Analysis: Calculated for CuSeC₂B₁₀H₁₁: C, 8.41; H, 3.88; found: C, 8.66; H, 3.79

Cu-[9-S-mCB] (**C**), off-white/light grey powder: 21 mg, 84%

Elemental Analysis: Calculated for CuSC₂B₁₀H₁₁: C, 10.06; H, 4.64; found: C, 10.31; H, 4.63

Cu-[9-S-oCB] (**D**), off-white/light grey powder: 17 mg, 69%

Elemental Analysis: Calculated for CuSC₂B₁₀H₁₁: C, 10.06; H, 4.63; found: C, 11.27; H, 4.86 (average of two duplicate runs). In the case of **D**, the experimental analysis deviates more significantly from the calculated values than the other three samples. However, when calculated with an impurity of *iso*-propanol (~10%), the calculated percent composition (C, 11.28; H, 4.86) matches the experimental data nearly exactly. These results suggest that the deviation between experimental and theoretical percent composition can be attributed to a small amount of *iso*-propanol impurity.

5. Supplementary Characterization and Data of A

a. Additional Electron Microscopy Images

Scanning Electron Microscopy

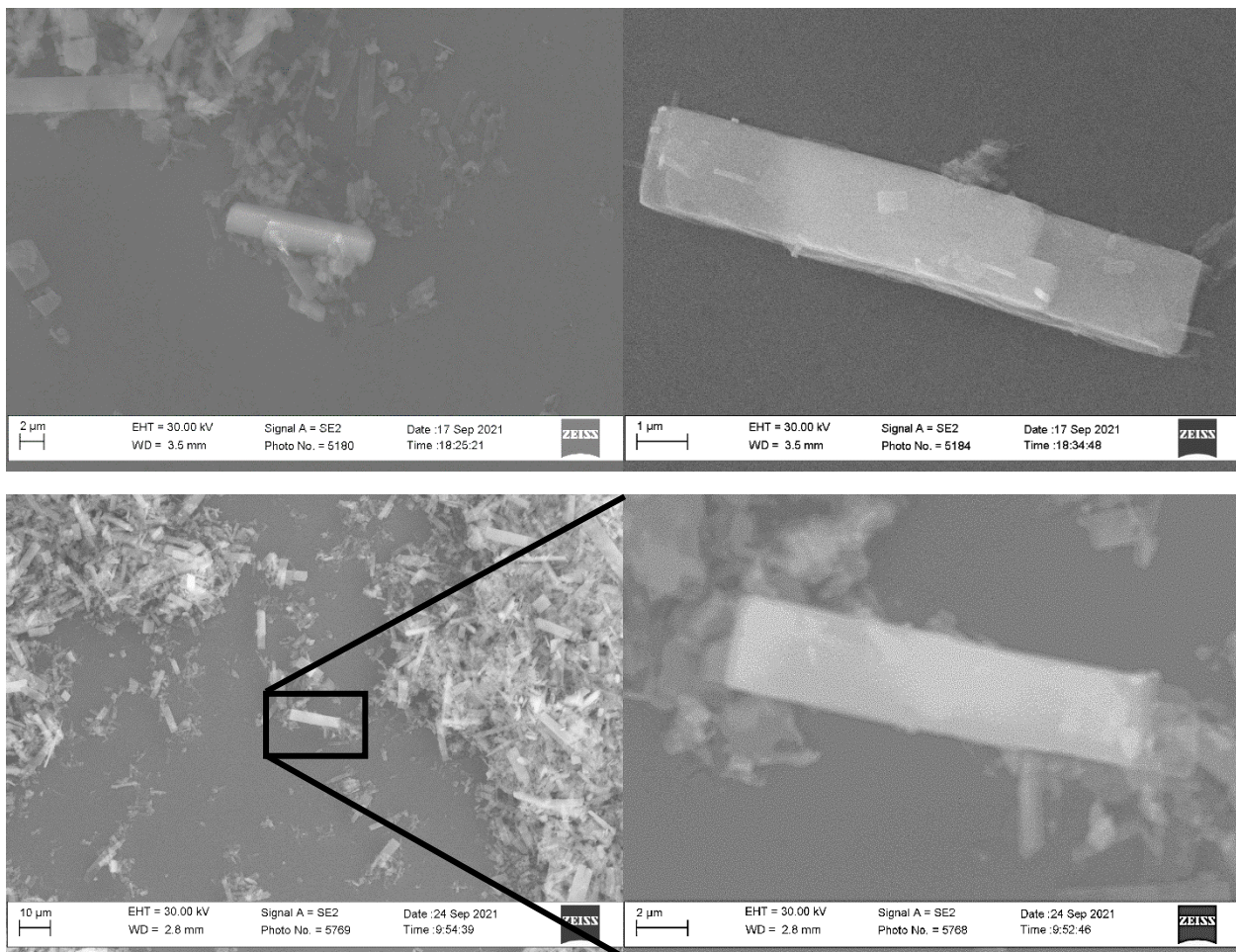


Figure S9: SEM images of A microcrystals deposited on a silicon wafer chip. SEM images reveal a consist crystallite morphology throughout the bulk material. Crystallites are typically between 5-10 μm in length and 1-2 μm in width. While there are some crystallites that exceed these dimensions, they maintain a consistent morphology of square rods.

Transmission Electron Microscopy

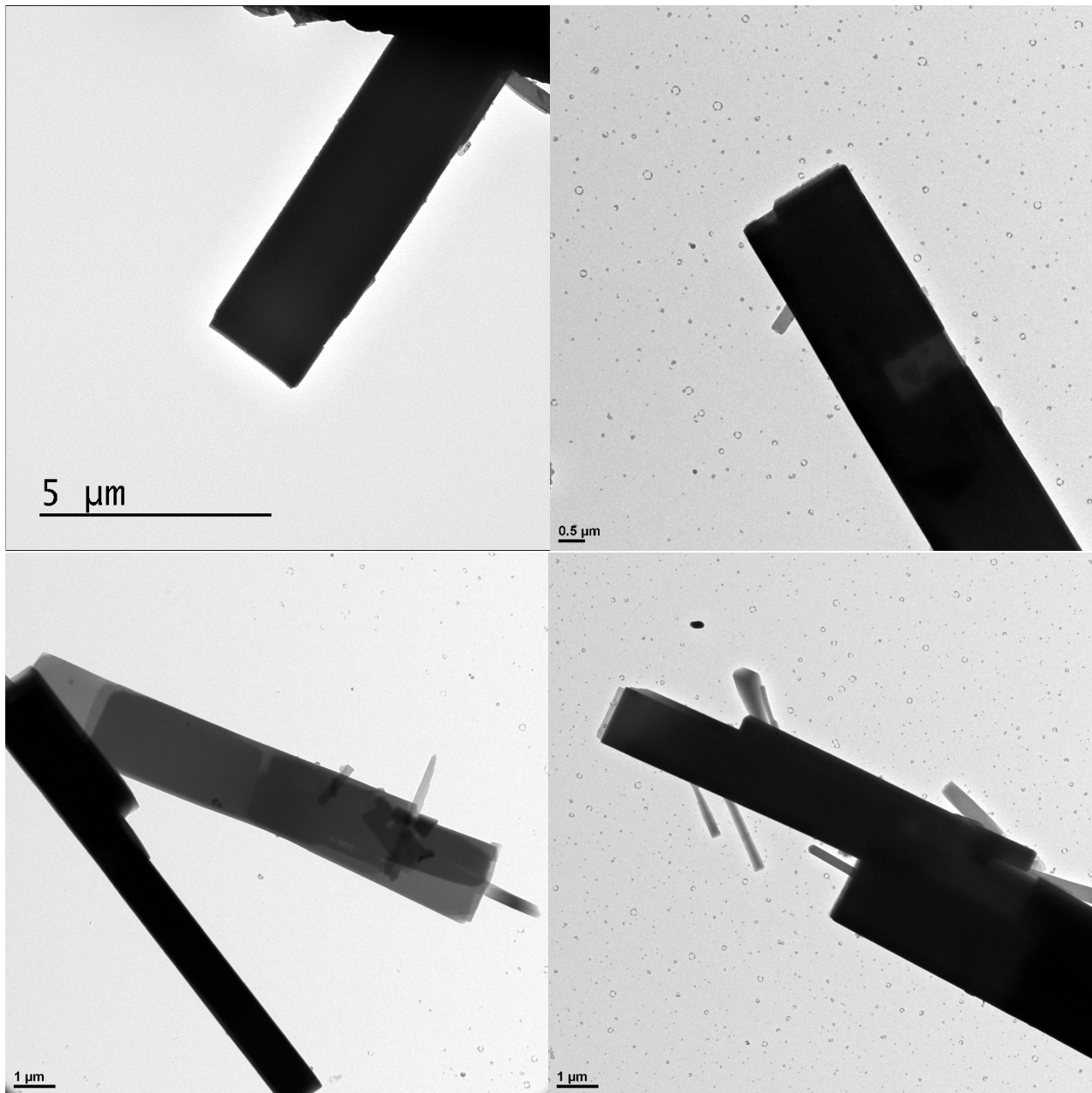


Figure S10: TEM images of A microcrystals deposited a copper grid (200 mesh, Formvar/Carbon or Carbon Film only). TEM images reveal the presence of rod-like microcrystals generally 5-10 μm in length and 1-2 μm in width. There is also evidence of smaller rods as shown in the bottom right TEM image.

b. Powder X-ray Diffraction Pattern

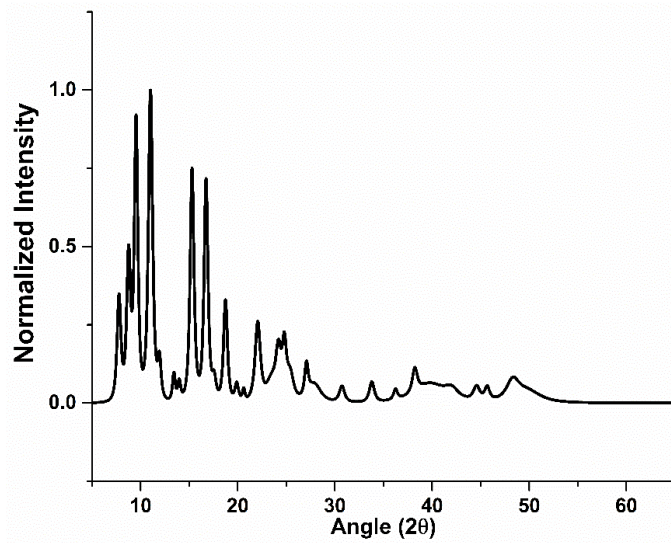


Figure S11: Powder X-ray diffraction pattern of A microcrystals deposited on a zero-background plate. Sample was diffracted from 5.000° to 65.000° with a step size of 0.016° . See included spreadsheet for peak list and corresponding intensities.

Cryo PXRD of A to Determine Effect of Thermal Contraction on PXRD Pattern

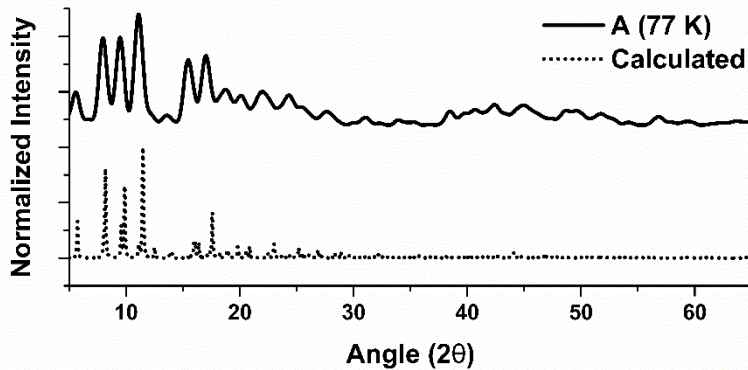


Figure S12: Stacked cryo (100K) and calculated from MicroED PXRD patterns.

When comparing the ambient temperature PXRD pattern of A with the calculated PXRD pattern determined from the MicroED structure, some deviations between the diffraction peaks was evident. To confirm that these differences were a result of thermal contraction/expansion from the two pieces of data obtained at separate temperatures, Cryo PXRD (depicted above) experiments were performed. The powder diffraction data were measured at 100K(2) on a Bruker Smart Apex2 CCD-based X-ray diffractometer system equipped with a micro-focus Cu-K α radiation ($\lambda = 1.54 \text{ \AA}$). A total of 5 frames were collected to cover the entire 2-theta range. The frames were integrated with the Bruker Pilot software package (Apex v2014) to obtain the raw data file to plot and analyze the data. Importantly, the diffractions peaks matched the calculated PXRD almost exactly, suggesting that the previously observed deviations are likely attributed to thermal contraction/expansion of the crystallites.

c. Infrared Spectroscopy

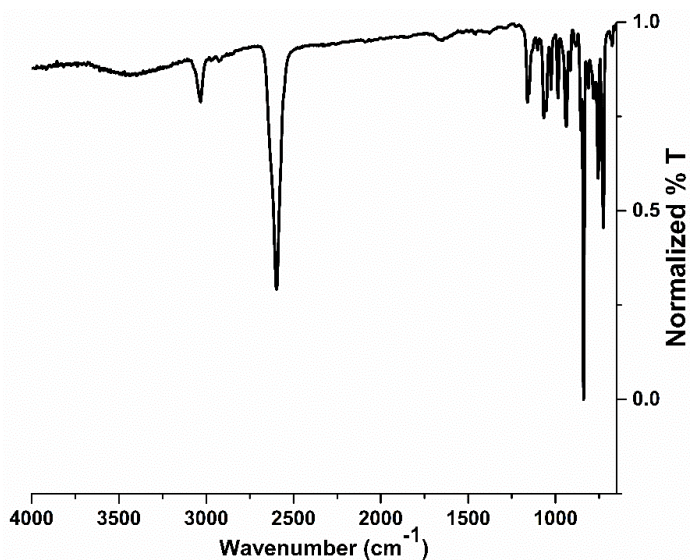


Figure S13: FTIR spectrum of A.

FTIR spectrum of A reveals no signals that could be correlated to residual starting material (CuOAC (C=O : $\sim 1500 \text{ cm}^{-1}$), HSe-mCB (H-Se: $\sim 2250 \text{ cm}^{-1}$), *iso*-propanol (H-C: $\sim 3000 \text{ cm}^{-1}$; H-O: $\sim 3500 \text{ cm}^{-1}$)). Two diagnostic resonances attributed to the carborane cluster (H-C_{carborane}: 3000 cm^{-1} ; H-B_{carborane}: 2700 cm^{-1}) are present and are expected to be symmetric as a function of the *meta*-carboranyl-selenolate symmetry.

d. Thermogravimetric Analysis

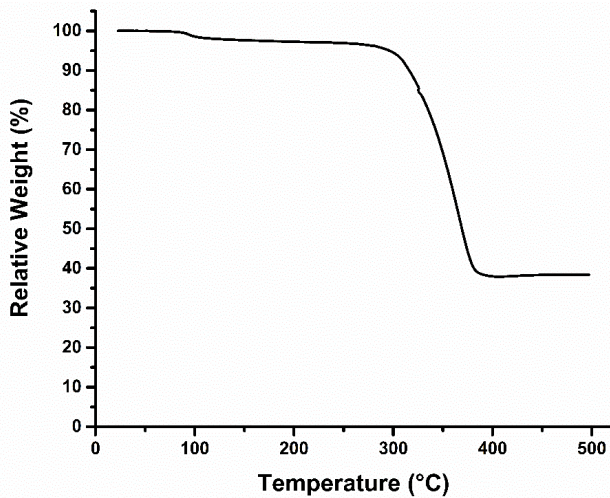


Figure S14: TGA of A.

TGA of A indicates the material is thermally stable until 300 $^{\circ}\text{C}$, after which, the material decomposes until reaching 40% relative weight at 375 $^{\circ}\text{C}$. There is no evident desolvation step that would indicate the presence of solvent adducts within the material, which would be expected near 100 $^{\circ}\text{C}$.

e. X-ray Photoelectron Spectroscopy

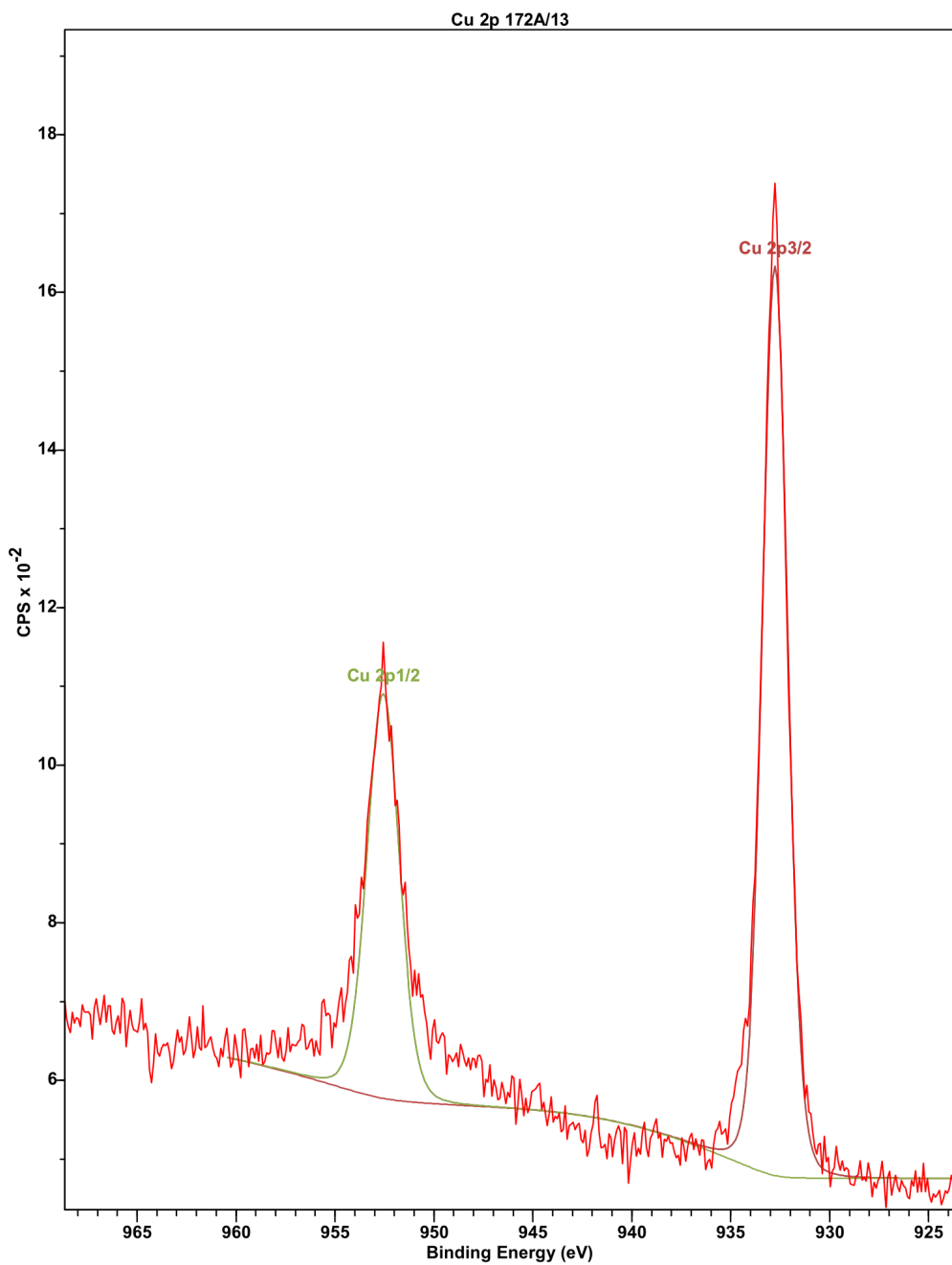


Figure S15: Cu 2p XPS region of A.

XPS data of A was processed and peak-fitted using CasaXPS. Peak fitting indicates the presence of only a single copper(I) environment, and is in agreement with all other structural characterization.

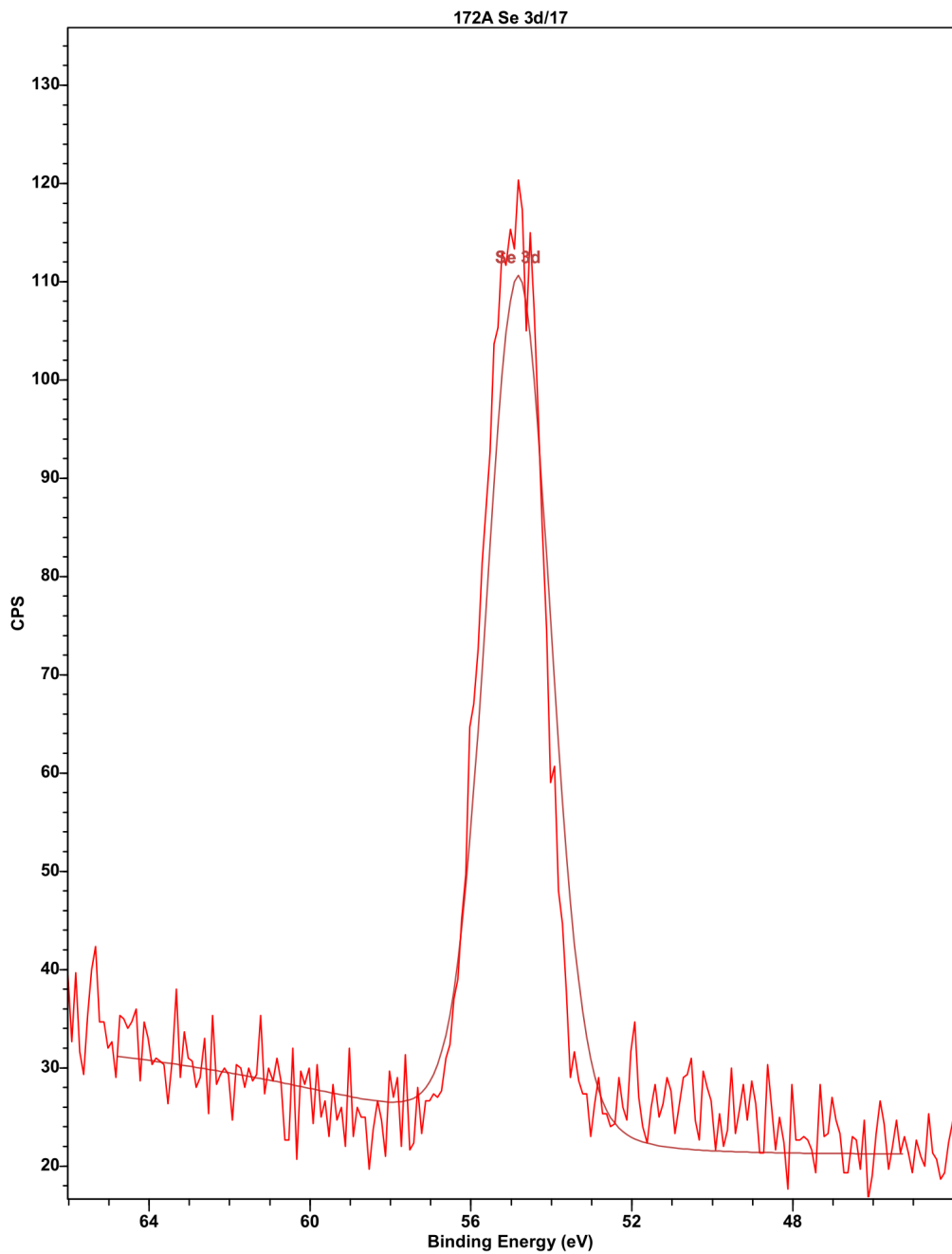


Figure S16: Se 3d XPS region of A.

XPS data of A was processed and peak-fitted using CasaXPS. Peak fitting indicates the presence of only a single selenolate environment, and is in agreement with all other structural characterization.

f. Photophysical Measurements

Absorption and Emission Measurements

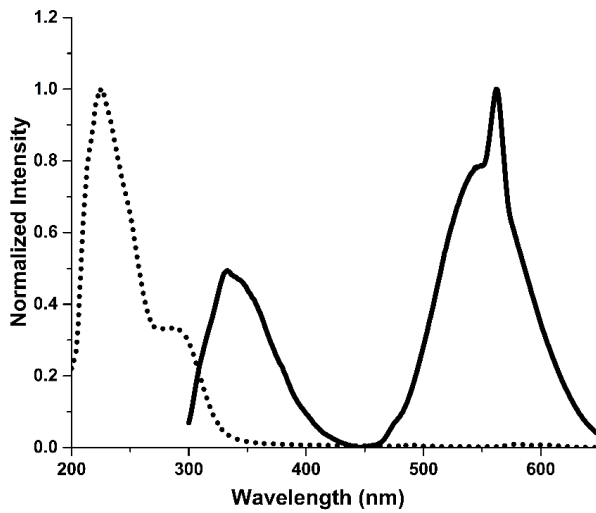


Figure S17: Absorption (dotted trace) and emission (solid trace) spectra of A.

Absorption (dotted trace) and emission (solid trace) of A have been normalized and plotted on the same set of axes. Both measurements were performed on suspension of A in *iso*-propanol. Emission spectrum was obtained by exciting the suspension with 280 nm light, and the emission was monitored between 300-650 nm. The sharp peak at 560 nm is an artifact of the excitation wavelength (280 nm), and is not a result of emission from A.

Comparison of Emission Intensity at Different Excitation Wavelengths

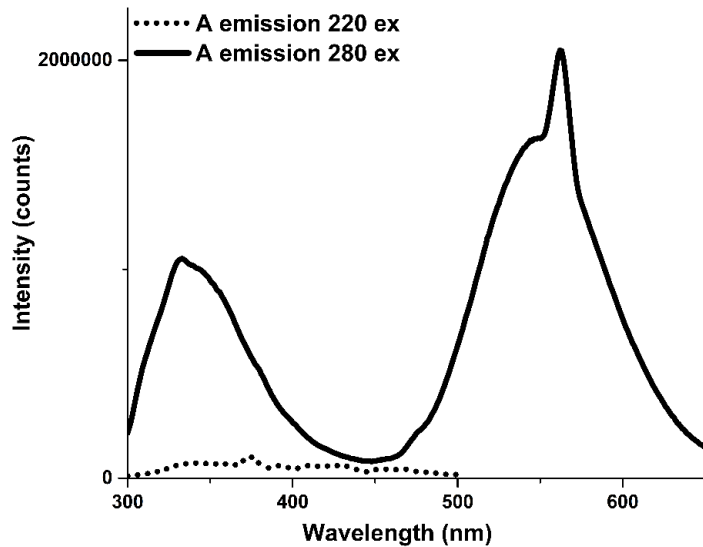


Figure S18: Comparison of emission intensity at different excitation wavelengths.

Emission traces when exciting a suspension of A in *iso*-propanol at 220 nm (dotted trace) and 280 nm (solid trace). Negligible emission can be correlated to excitation at 220 nm.

Quantum Yields

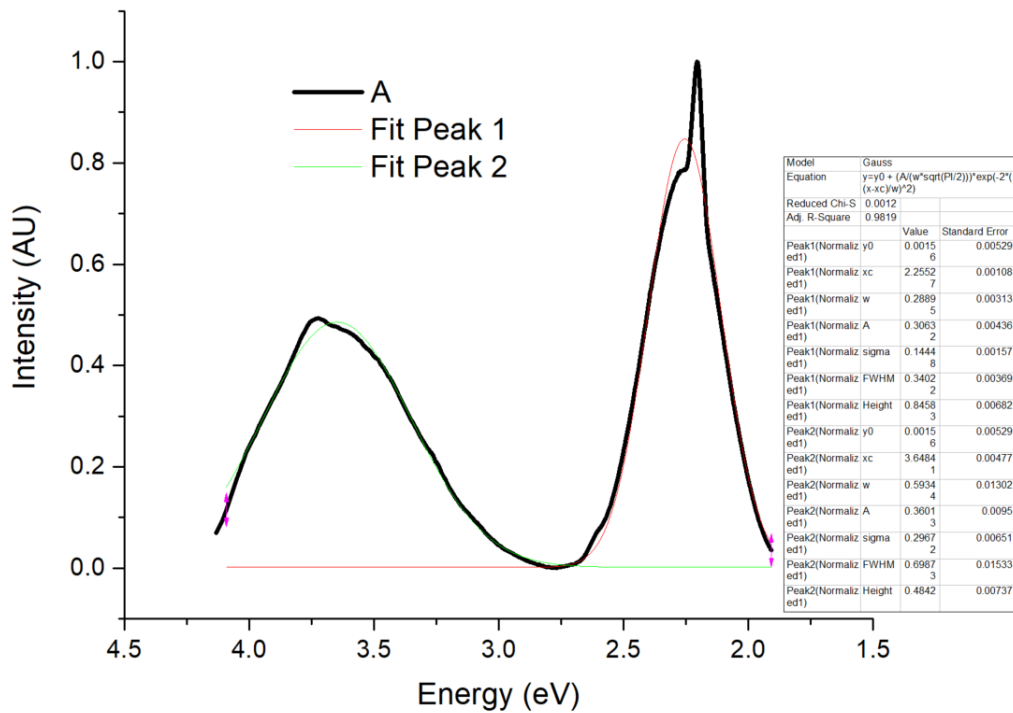


Figure S19: Peak fitting of A emission used to determine the relative peak integrations of the high (54%) and low (46%) energy transitions.

Lifetime Measurements

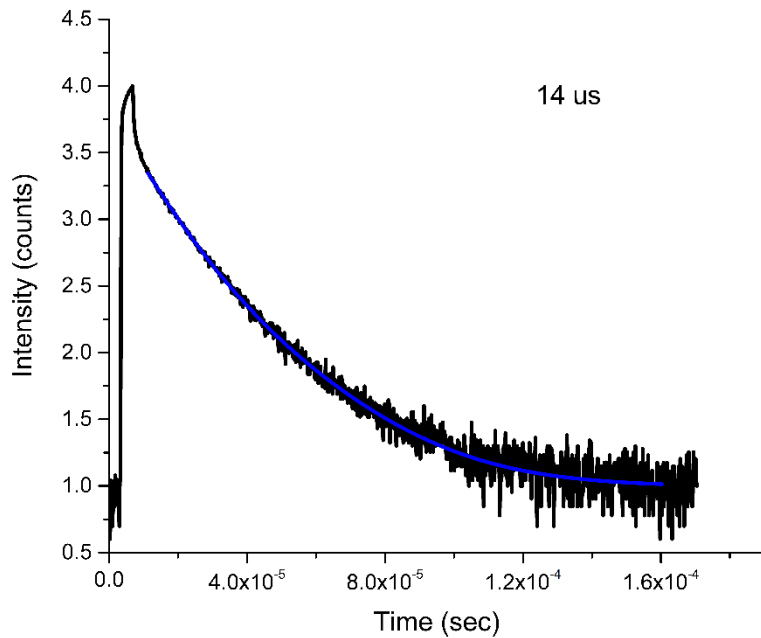


Figure S20: Lifetime plot of A, indicating a lifetime emission of 14 μ s.

g. DFT Calculations

DFT calculations of **A** were performed using B3LYP functional with DZP basis set. The crystallographically derived structure by MicroED was used for calculations of the molecular orbitals of **A**. The calculated HOMO-LUMO gap is 4.35 eV, corresponding to 285 nm.

Atomic Coordinates:

B	-4.46822700	9.01069500	18.61489900	B	3.56649000	8.26239800	22.42978100
B	2.67677300	9.14329000	13.97659400	B	-1.44958400	9.63446800	20.04894900
C	1.40147700	1.08382000	19.78681100	C	4.23724700	6.82576000	14.39293100
B	3.75695800	9.43154000	25.08508800	B	2.14388000	8.67056000	24.91546900
Se	3.12285800	8.50222200	18.31883700	B	-3.52080000	7.72164100	19.42598600
Se	-0.69886300	6.62975000	19.00656400	C	-4.19295700	9.05450900	20.34192700
Cu	1.19179600	7.61441200	18.77218200	B	4.34832100	8.54373000	14.09995300
B	3.06332300	8.08253000	16.55480100	B	0.60838600	2.06617600	18.58405900
B	3.48353900	6.50292000	15.95034100	C	4.56008700	9.19517500	23.54926600
B	3.19123100	2.90440700	17.67120100	H	4.98652400	6.18008000	14.04444200
C	-3.28887600	10.13487000	17.97343100	H	0.70864300	7.71357000	13.73912800
C	1.64189100	7.74816000	14.21714500	H	0.82702400	0.50732000	20.45603500
B	2.92167000	0.45428200	19.18851900	H	3.59027200	0.63415000	16.84161100
C	2.34608400	10.39198900	24.66875000	H	5.60412300	9.08564000	23.51225800
B	-2.96256200	10.22480400	20.77985200	H	1.95299500	11.06880000	25.37498200
B	3.10836100	7.55215000	13.27036300	H	-4.99397600	8.87810000	21.00189900
B	1.49566000	0.58803000	18.09987400	H	-3.50563200	10.66525000	17.08832900
B	3.86260000	10.76556100	23.87308400	H	1.21329880	4.55124948	18.03426446
B	-4.11272500	10.56263300	19.45990900	H	0.97645698	3.64404127	20.68729267
B	1.66406300	2.12152000	17.17159700	H	-0.57788637	2.13620653	18.50576360
B	3.73986800	10.02994700	22.24474300	H	3.32730396	1.70452228	21.43648619
B	-2.37503300	10.92236900	19.24403100	H	5.11632103	1.96134113	19.24200738
B	2.56511100	6.28385000	14.42993900	H	3.38467358	-0.59713361	19.50125489
C	3.07051400	1.15300000	17.59410200	H	1.08300532	-0.28661754	17.39941833
B	2.31381200	10.80130400	22.96947800	H	3.75676724	3.76550436	17.06947936
B	2.13885600	9.27012000	22.08437600	H	1.26563348	2.22851144	16.05513101
B	-1.65209500	9.60449000	18.27874500	H	-4.94569154	11.34103548	19.81427006
Se	4.07544500	4.64428400	20.12296500	H	-3.90091593	6.59685371	19.52087693
Cu	3.46166800	6.50637900	19.21627500	H	-5.39629337	8.84360624	17.88005707
B	3.01124800	3.25261300	19.35813800	H	-3.41012589	8.10153648	16.85806986
B	1.81745700	7.10248000	15.83623400	H	-2.08084574	7.84781518	21.64067151
B	3.96986500	1.87939000	18.91712900	H	-0.38277667	9.82436143	20.53899804
B	1.25105000	9.51916800	23.61402900	H	-2.99342150	10.84923110	21.79282831
B	-2.94758200	8.42843000	17.89324800	H	-0.74201764	9.80177943	17.53641460
Se	1.18177600	6.34495900	23.00648500	H	-1.86410918	11.99125588	19.39687578
Cu	2.56444700	5.49404500	21.51383900	H	3.80896452	5.43441895	16.37450674
B	2.09148000	8.04217500	23.30563100	H	1.94917826	5.30598957	14.12810262
B	1.87898600	8.86657000	15.55559200	H	3.40587408	7.35456458	12.13103978
B	2.89547700	1.82174000	20.33267500	H	5.30797584	9.05590660	13.57226127
Cu	0.29477800	6.57210000	21.01423500	H	2.11920473	10.00854801	13.36473020
B	-1.86125400	8.17131100	19.22244300	H	3.94015672	10.40617644	15.88537625
B	3.58421200	9.33930000	15.49391200	H	1.23402597	9.67514048	16.14998230
B	1.45583300	2.82485000	19.96259800	H	0.92888442	6.57742719	16.42525283
B	3.57325900	7.90266200	24.18456600	H	5.64474423	7.94354013	16.29567166
B	-2.59289500	8.47339700	20.76134900	H	3.98832985	6.85339983	24.56834531
B	4.58868500	7.89805000	15.74679800	H	4.50354687	11.78241792	23.95253690
B	1.64885800	3.48321300	18.31883700	H	1.97357490	11.93316070	22.77050855

H	1.58025130	8.17737769	25.84094306	H	4.01843285	7.48395087	21.65332006
H	4.31110459	9.49062940	26.13875402	H	4.28522433	10.33224774	21.24294425
H	0.05096366	9.66278452	23.54141361	H	2.26418057	9.67616380	20.98354805

6. Supplementary Characterization and Data of B

a. Additional Electron Microscopy Images

Scanning Electron Microscopy

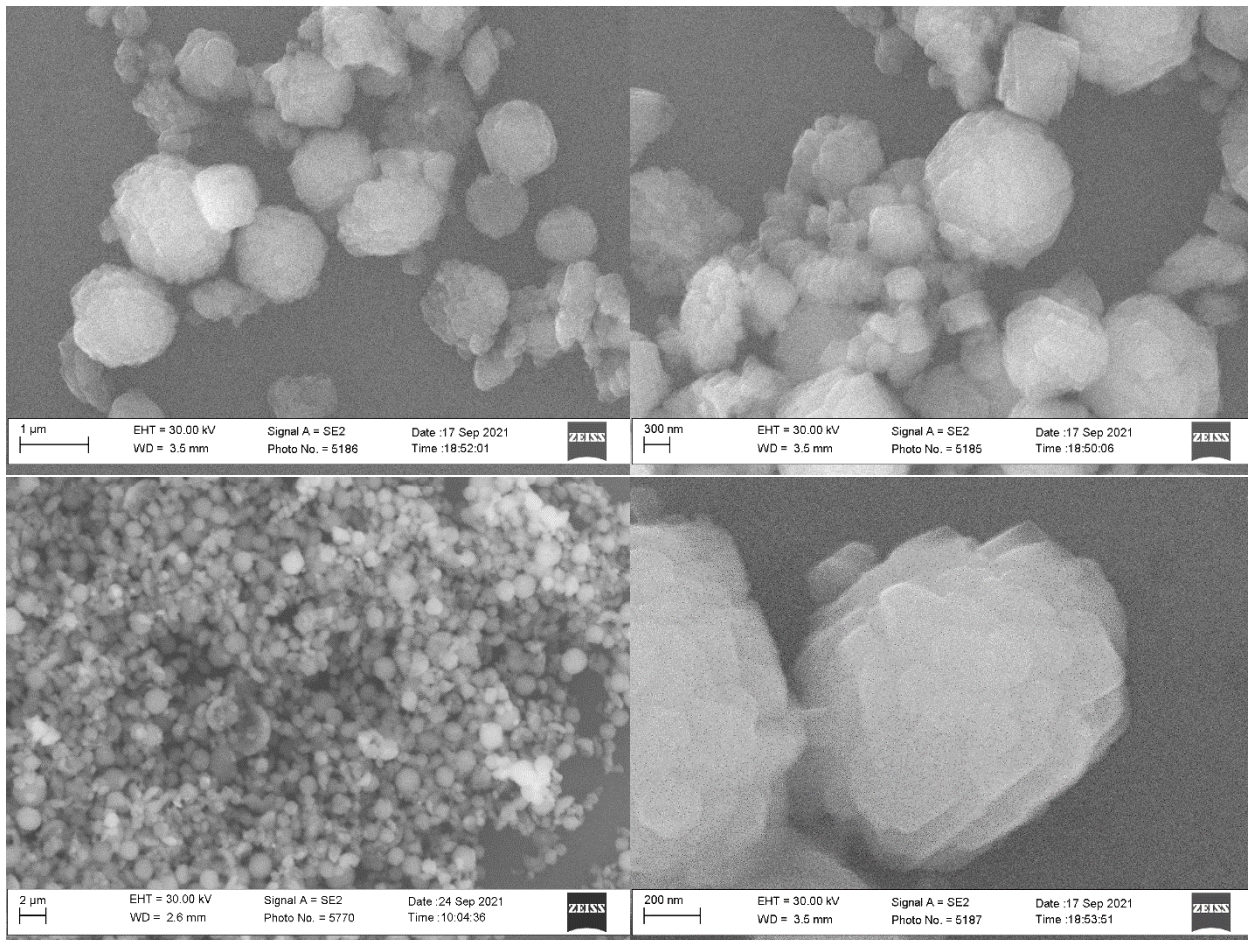


Figure S21: SEM images of **B** microcrystals deposited on a silicon wafer chip. SEM images reveal a microscale particle phase present in bulk **B**. The upper two images were used to determine the average microscale particle size to be $1.10 \mu\text{m} \pm 0.31$ in diameter. While spherical in nature, in higher magnification images (bottom right), the particles appear to be comprised of platelets stacked on top of one another.

Transmission Electron Microscopy

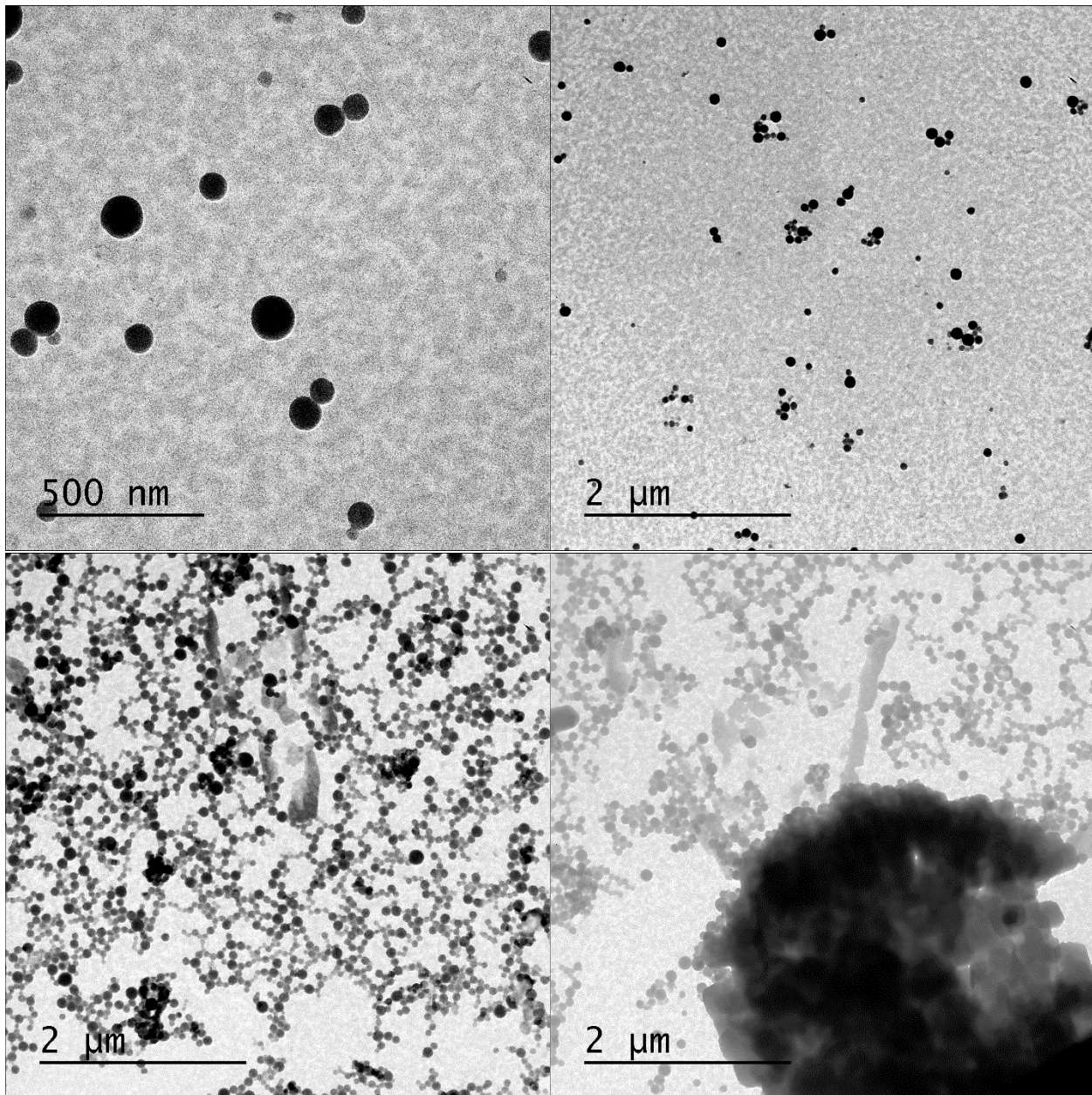


Figure S22: TEM images of **B** microcrystals deposited a copper grid (200 mesh, Formvar/Carbon or Carbon Film only). TEM images reveal the presence of spherical nanoparticles comingled with the larger aggregates observed by SEM (bottom right). The upper two images were used to determine the average nanoparticle size to be $92 \text{ nm} \pm 25 \text{ nm}$ in diameter.

b. Powder X-ray Diffraction Pattern

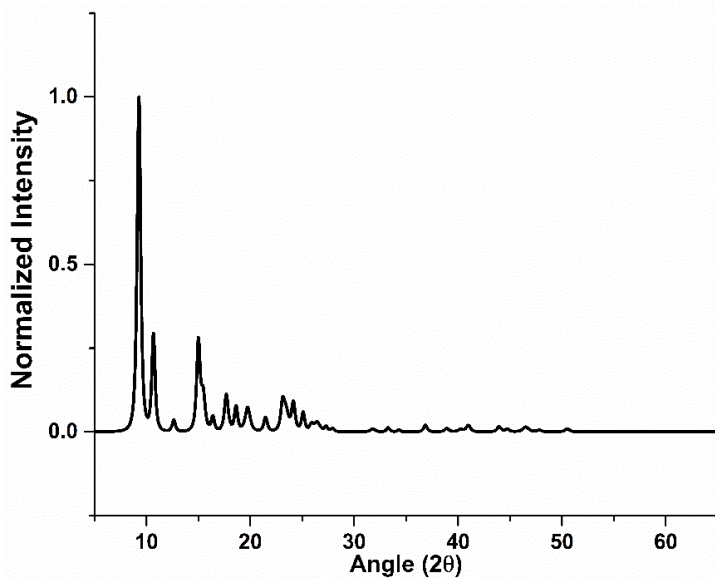


Figure S23: Powder X-ray diffraction pattern of **B** microcrystals deposited on a zero-background plate. Sample was diffracted from 5.000° to 65.000° with a step size of 0.016° . See included spreadsheet for peak list and corresponding intensities.

c. Infrared Spectroscopy

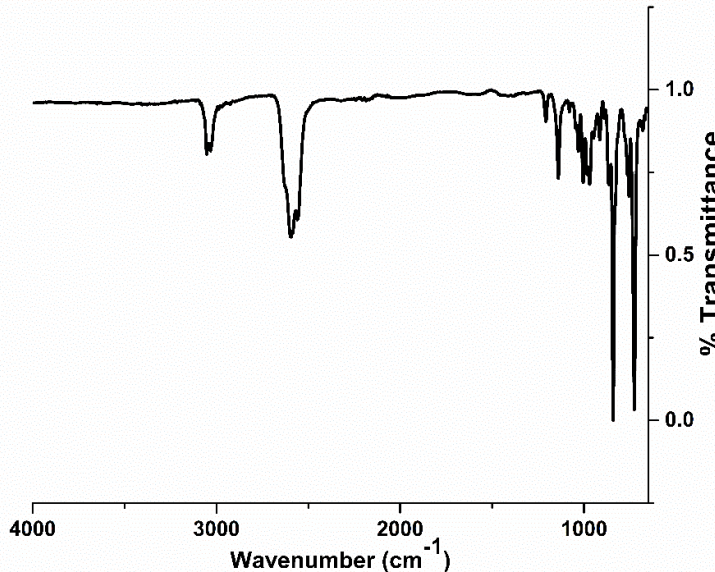


Figure S24: FTIR spectrum of **B**.

FTIR spectrum of **B** reveals no signals that could be correlated to residual starting material (CuOAC (C=O : $\sim 1500 \text{ cm}^{-1}$), HSe-oCB (H-Se: $\sim 2250 \text{ cm}^{-1}$), *iso*-propanol (H-C: $\sim 3000 \text{ cm}^{-1}$; H-O: $\sim 3500 \text{ cm}^{-1}$)). Two diagnostic resonances attributed to the carborane cluster (H-C_{carborane}: 3000 cm^{-1} ; H-B_{carborane}: 2500 cm^{-1}) are present and are expected to be slightly asymmetric as a function of the *ortho*-carboranyl-selenolate asymmetry.

d. Thermogravimetric Analysis

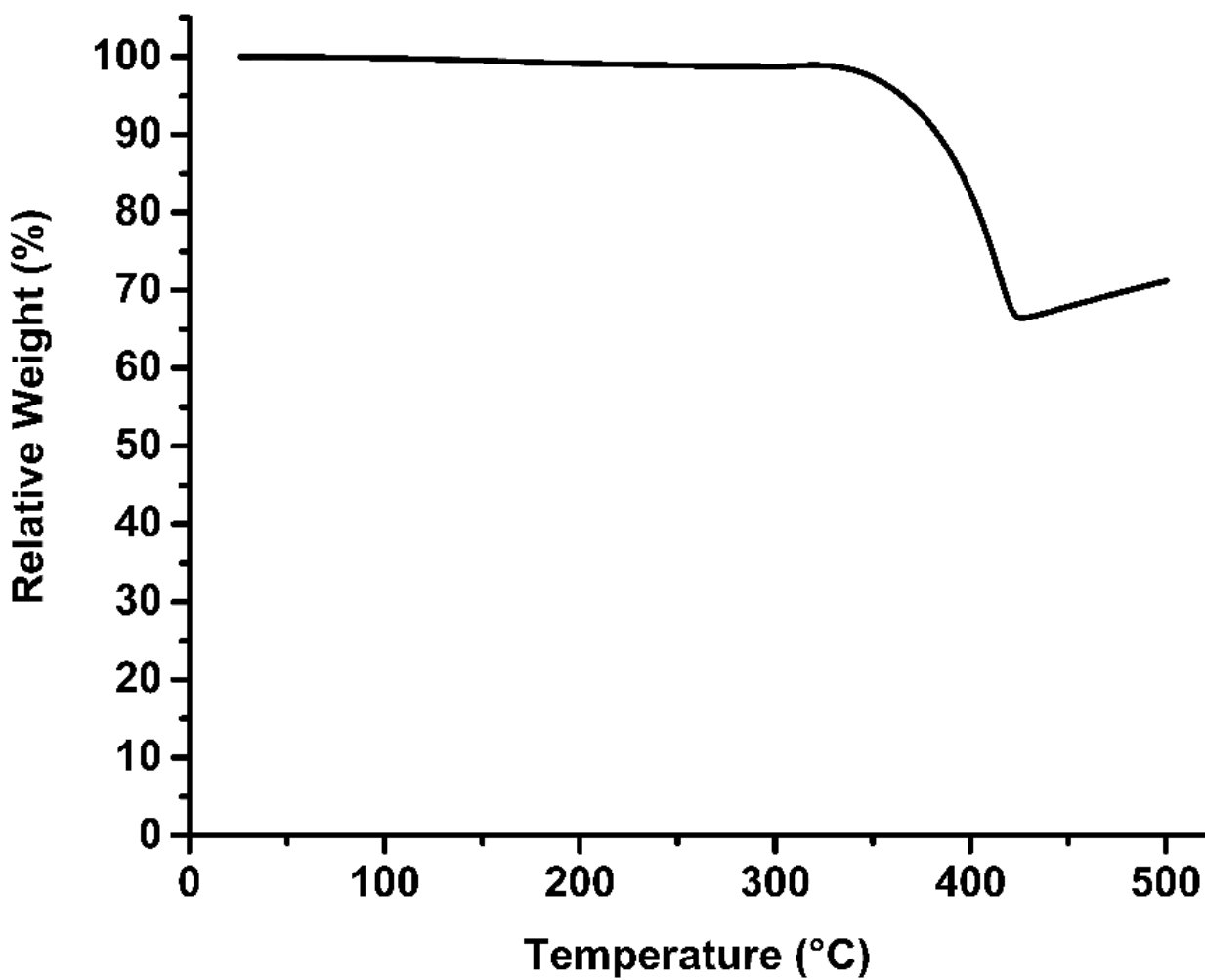


Figure S25: TGA of **B**.

TGA of **B** indicates the material is thermally stable until 350 °C, after which, the material decomposes until reaching 65% relative weight at 400 °C. There is no evident desolvation step that would indicate the presence of solvent adducts within the material, which would be expected near 100 °C.

e. X-ray Photoelectron Spectroscopy

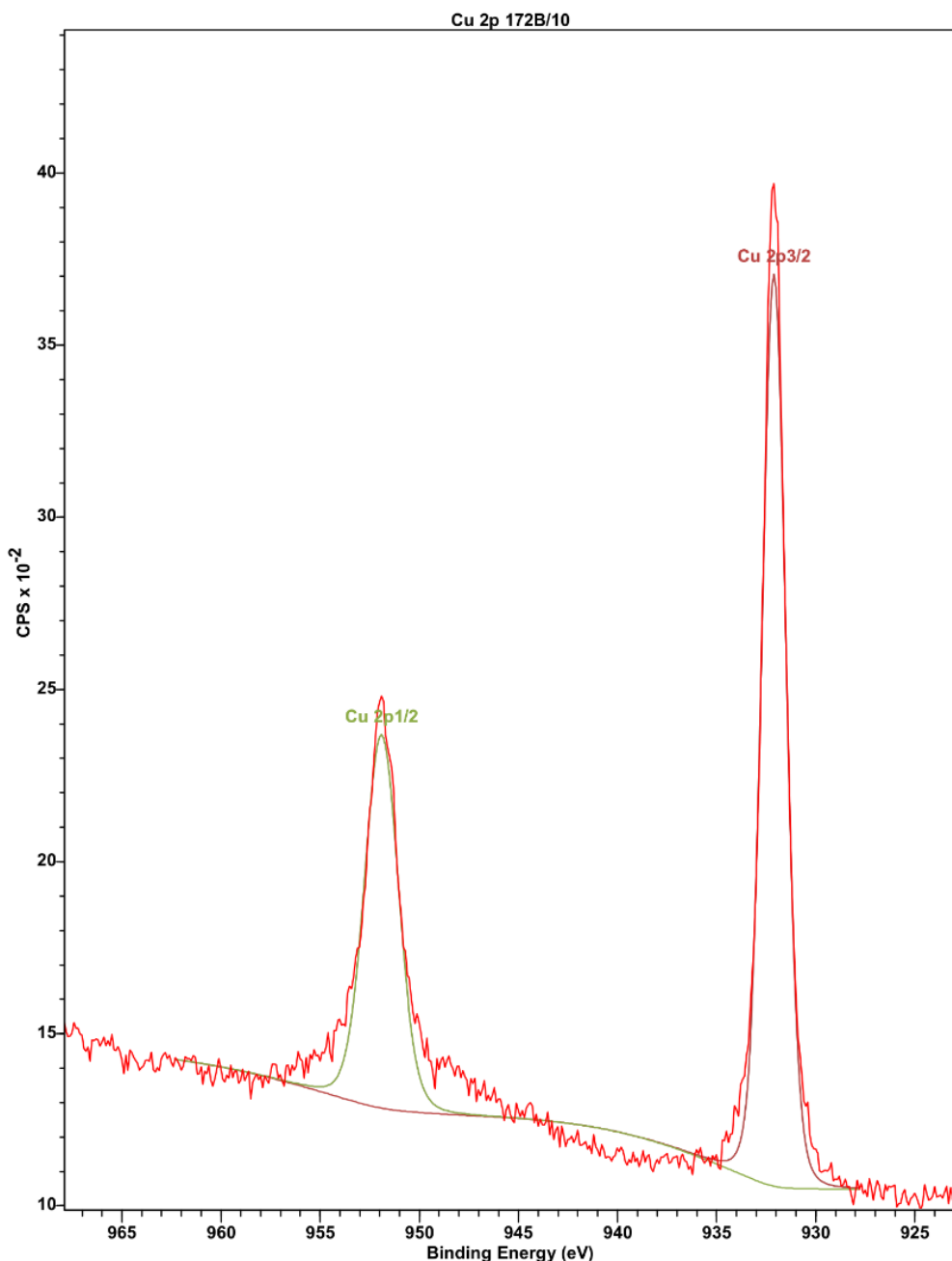


Figure S26: Cu 2p XPS region of **B**.

XPS data of **B** was processed and peak-fitted using CasaXPS. Peak fitting indicates the presence of only a single copper(I) environment, and is in agreement with all other structural characterization.

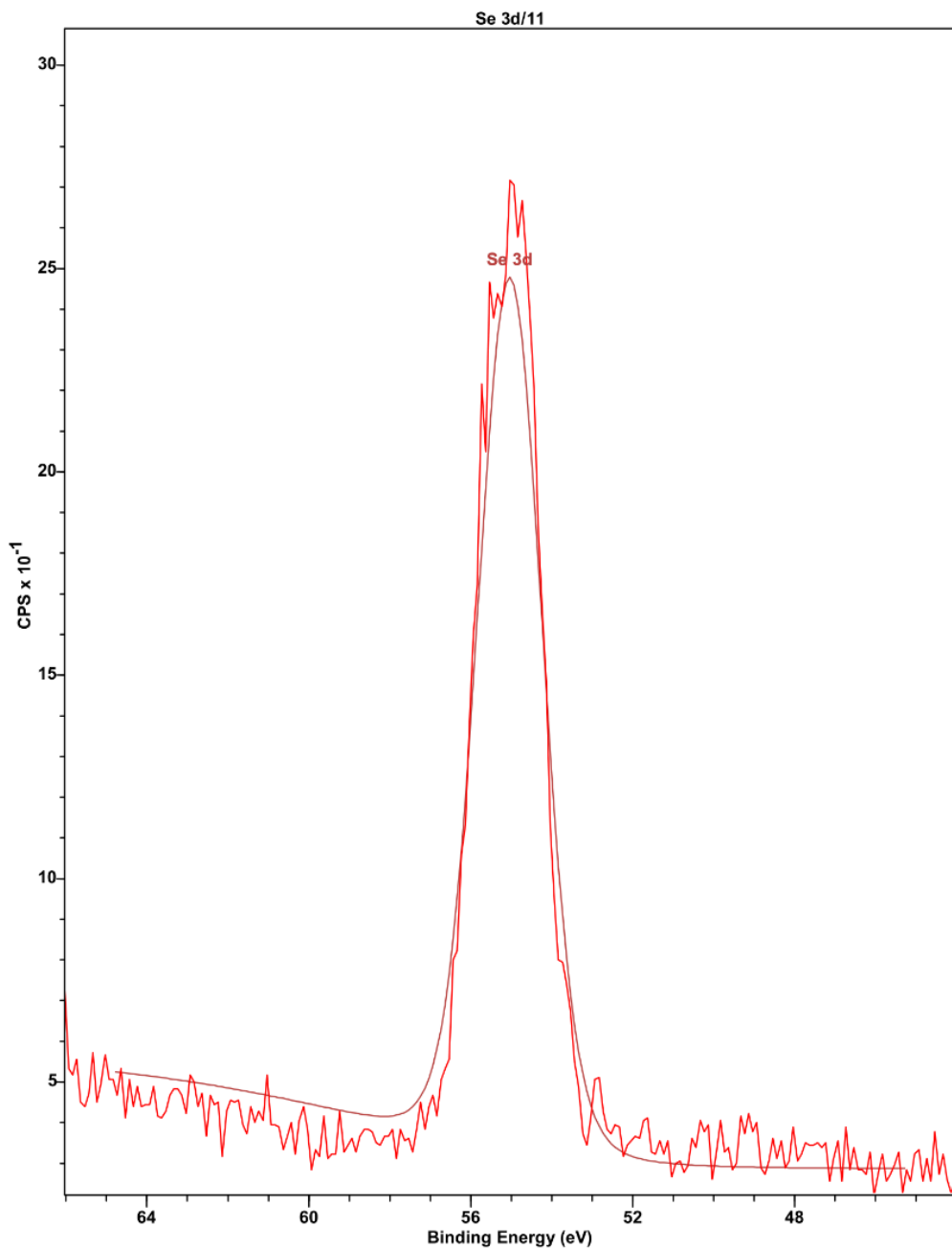


Figure S27: Se 3d XPS region of **B**.

XPS data of **B** was processed and peak-fitted using CasaXPS. Peak fitting indicates the presence of only a single selenolate environment, and is in agreement with all other structural characterization.

f. Photophysical Measurements

Absorption and Emission Measurements

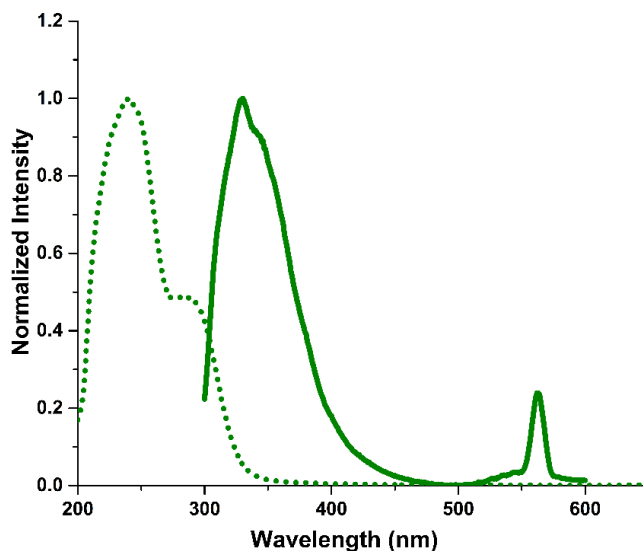


Figure S28: Absorption (dotted trace) and emission (solid trace) spectra of **B**.

Absorption (dotted trace) and emission (solid trace) of **B** have been normalized and plotted on the same set of axes. Both measurements were performed on suspension of **B** in *iso*-propanol. Emission spectrum was obtained by exciting the suspension with 280 nm light, and the emission was monitored between 300-600 nm. The sharp peak at 560 nm is an artifact of the excitation wavelength (280 nm), and is not a result of emission from **B**.

Comparison of Emission Intensity at Different Excitation Wavelengths

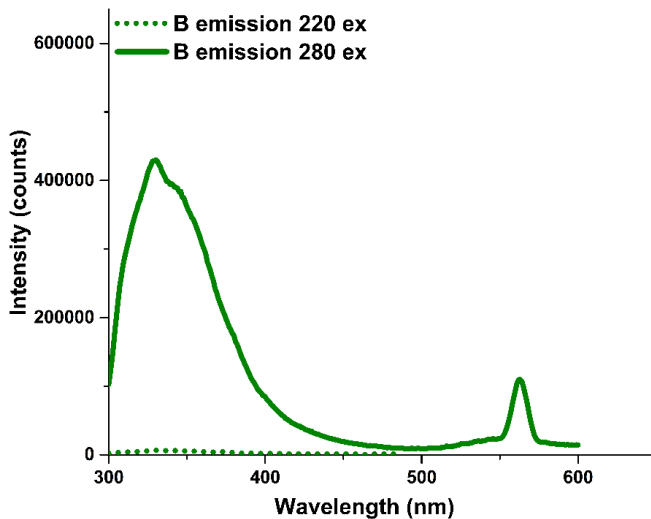


Figure S29: Comparison of emission intensity at different excitation wavelengths.

Emission traces when exciting a suspension of **B** in *iso*-propanol at 220 nm (dotted trace) and 280 nm (solid trace). Negligible emission can be correlated to excitation at 220 nm.

Lifetime Measurements

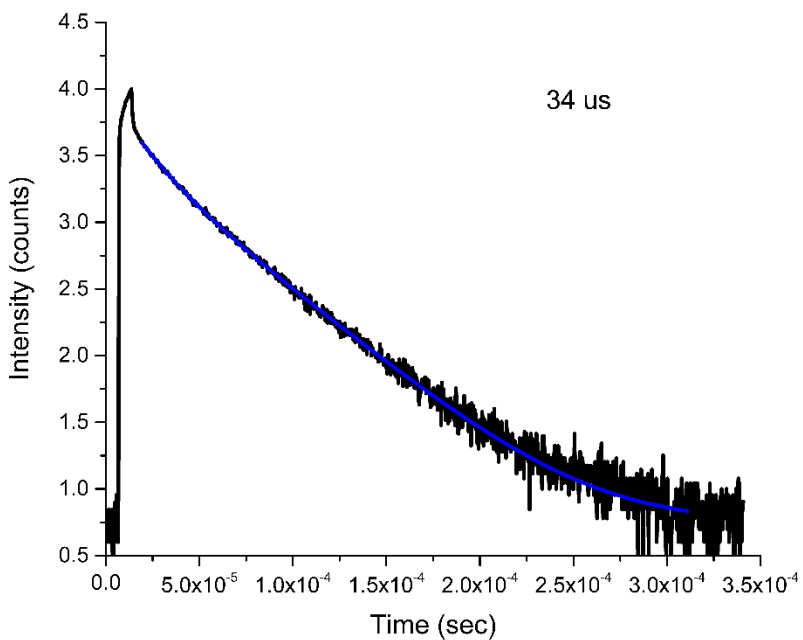


Figure S30: Lifetime plot of **B**, indicating a lifetime emission of 34 μs .

g. Attempted MicroED

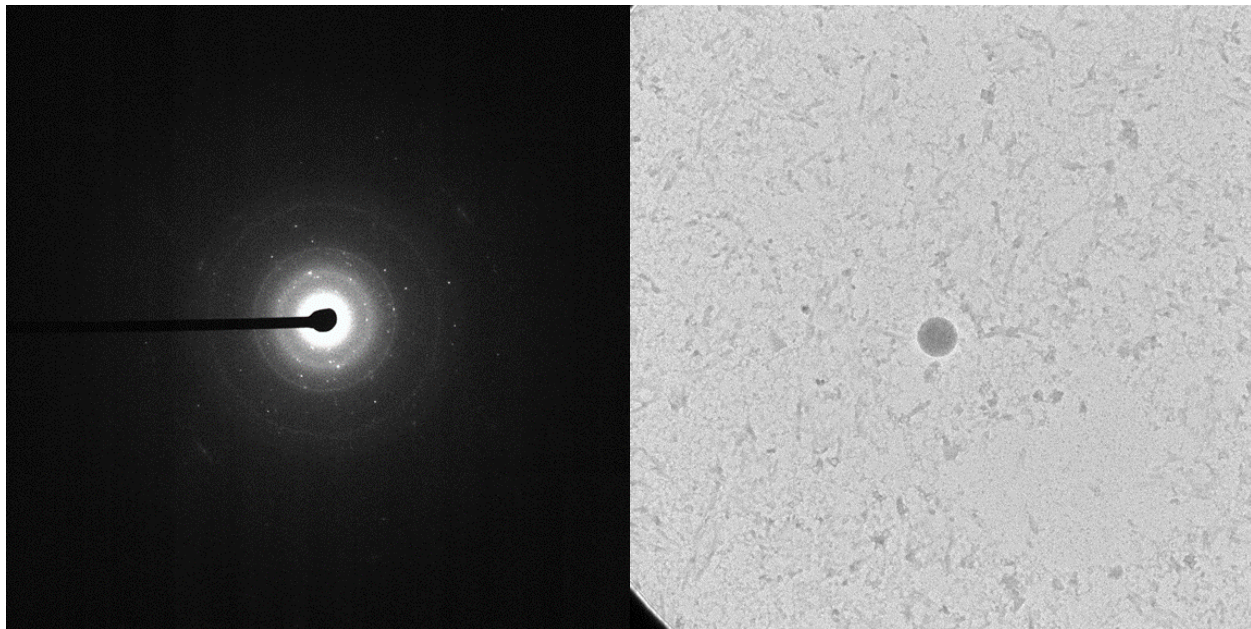


Figure S31: SAED and bright field image of **B** microcrystal on TEM grid.

MicroED was attempted using the previously described method outlined above. Selected Area Electron Diffraction (SAED, left image) confirmed the presence of crystalline material, however the majority of the observed diffractions were polycrystalline in nature and thus were not sufficient for single crystal analysis using MicroED.

7. Supplementary Characterization and Data of C

a. Additional Electron Microscopy Images

Scanning Electron Microscopy

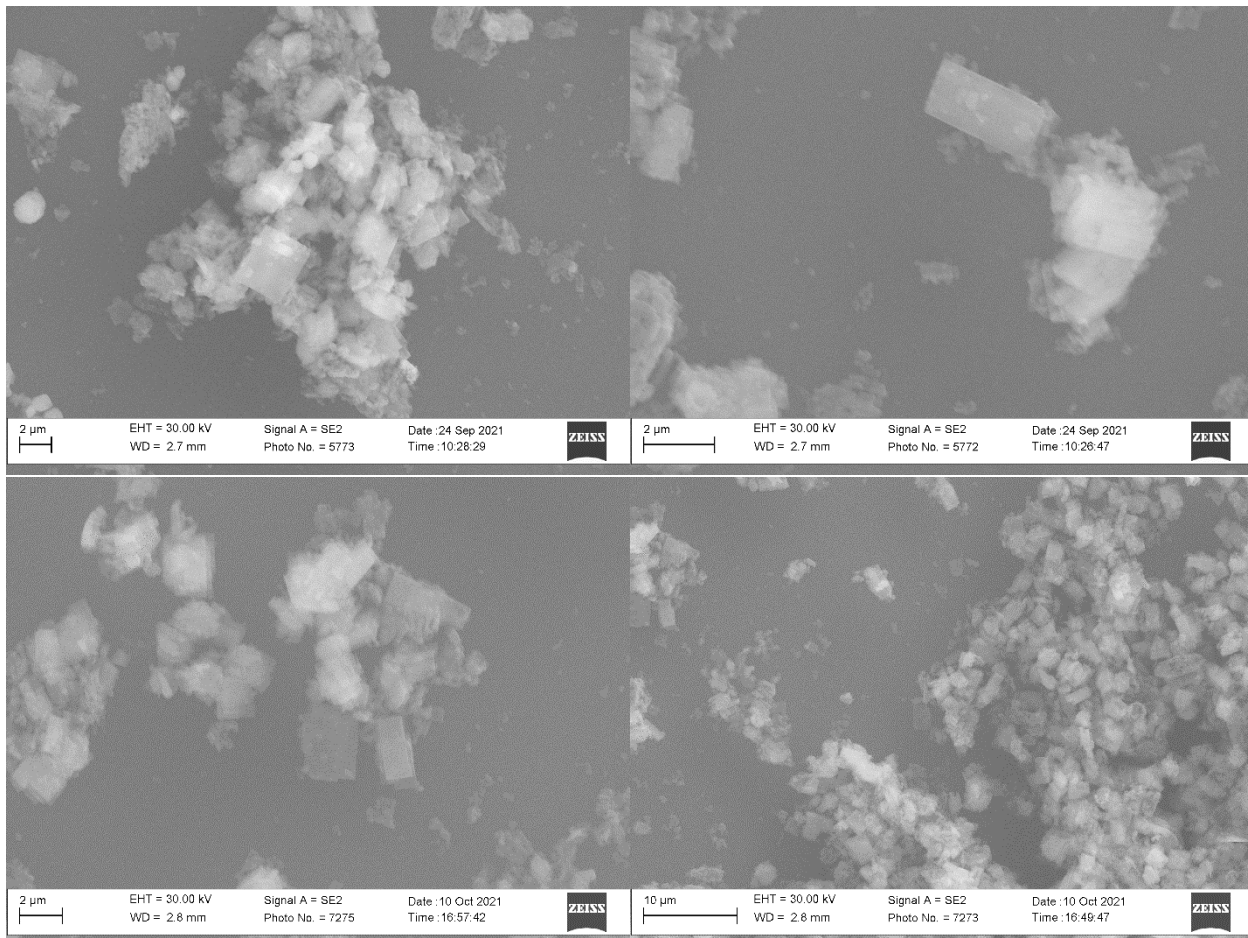


Figure S32: SEM images of C microcrystals deposited on a silicon wafer chip. SEM images reveal a consistent crystallite morphology throughout the bulk material. Crystallites are typically between 3-5 μm in length and 2-3 μm in width. While there are some crystallites that exceed these dimensions, they maintain a consistent morphology of square prisms.

Transmission Electron Microscopy

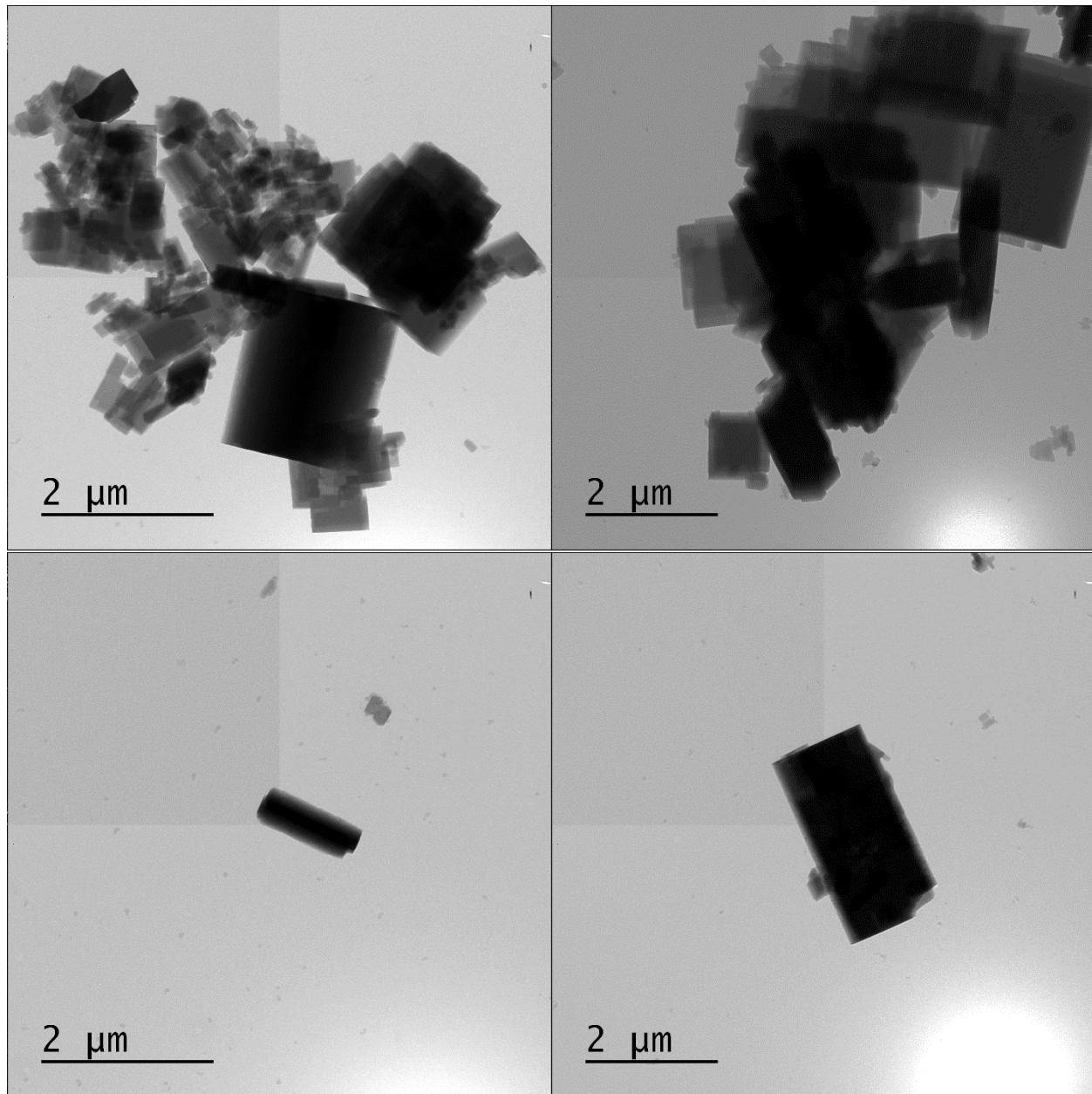


Figure S33: TEM images of C microcrystals deposited a copper grid (200 mesh, Formvar/Carbon or Carbon Film only). TEM images reveal the presence of cubic crystallites, in agreement with morphology observed by SEM.

b. Powder X-ray Diffraction Pattern

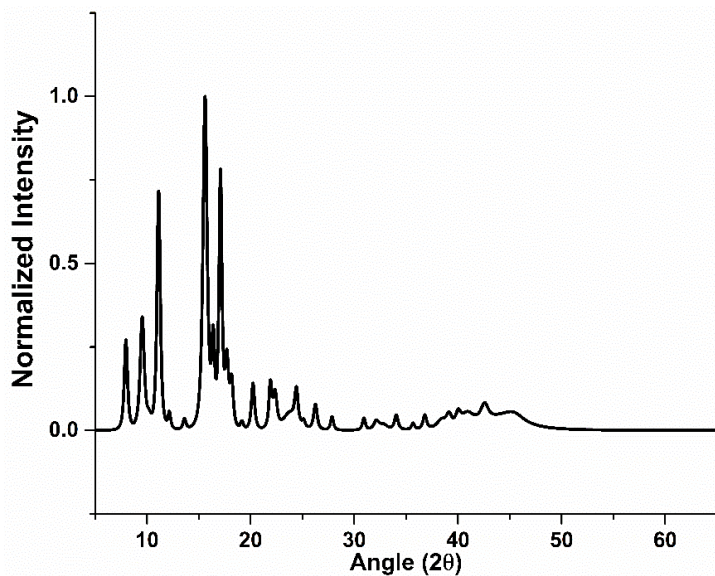


Figure S34: Powder X-ray diffraction pattern of **C** microcrystals deposited on a zero-background plate. Sample was diffracted from 5.000° to 65.000° with a step size of 0.016°. See included spreadsheet for peak list and corresponding intensities.

c. Infrared Spectroscopy

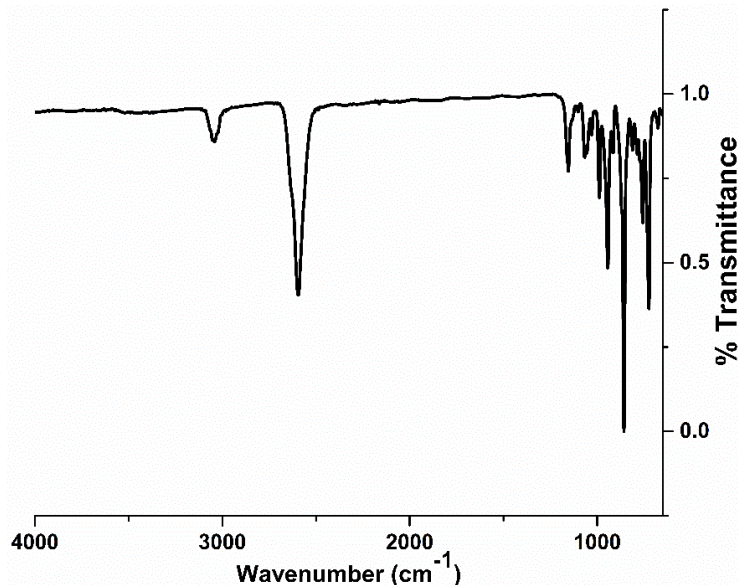


Figure S35: FTIR spectrum of **C**.

FTIR spectrum of **C** reveals no signals that could be correlated to residual starting material (CuOAC (C=O : $\sim 1500 \text{ cm}^{-1}$), HS-mCB (H-S: $\sim 2500 \text{ cm}^{-1}$), *iso*-propanol (H-C: $\sim 3000 \text{ cm}^{-1}$; H-O: $\sim 3500 \text{ cm}^{-1}$)). Two diagnostic resonances attributed to the carborane cluster (H-C_{carborane}: 3000 cm^{-1} ; H-B_{carborane}: 2600 cm^{-1}) are present and are expected to be symmetric as a function of the *meta*-carboranyl-thiolate symmetry.

d. Thermogravimetric Analysis

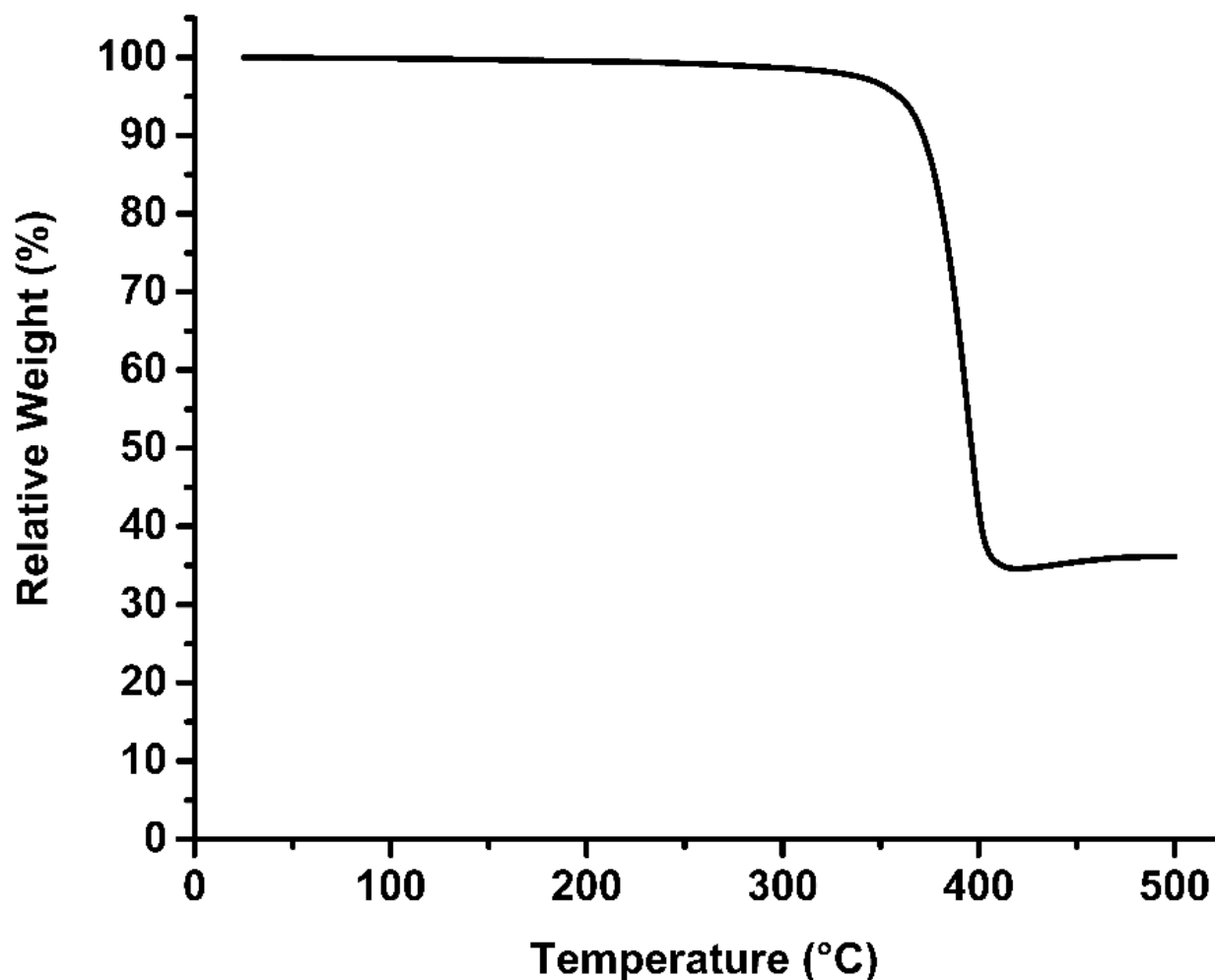


Figure S36: TGA of C.

TGA of C indicates the material is thermally stable until 350 °C, after which, the material decomposes until reaching 40% relative weight at 400 °C. There is no evident desolvation step that would indicate the presence of solvent adducts within the material, which would be expected near 100 °C.

e. X-ray Photoelectron Spectroscopy

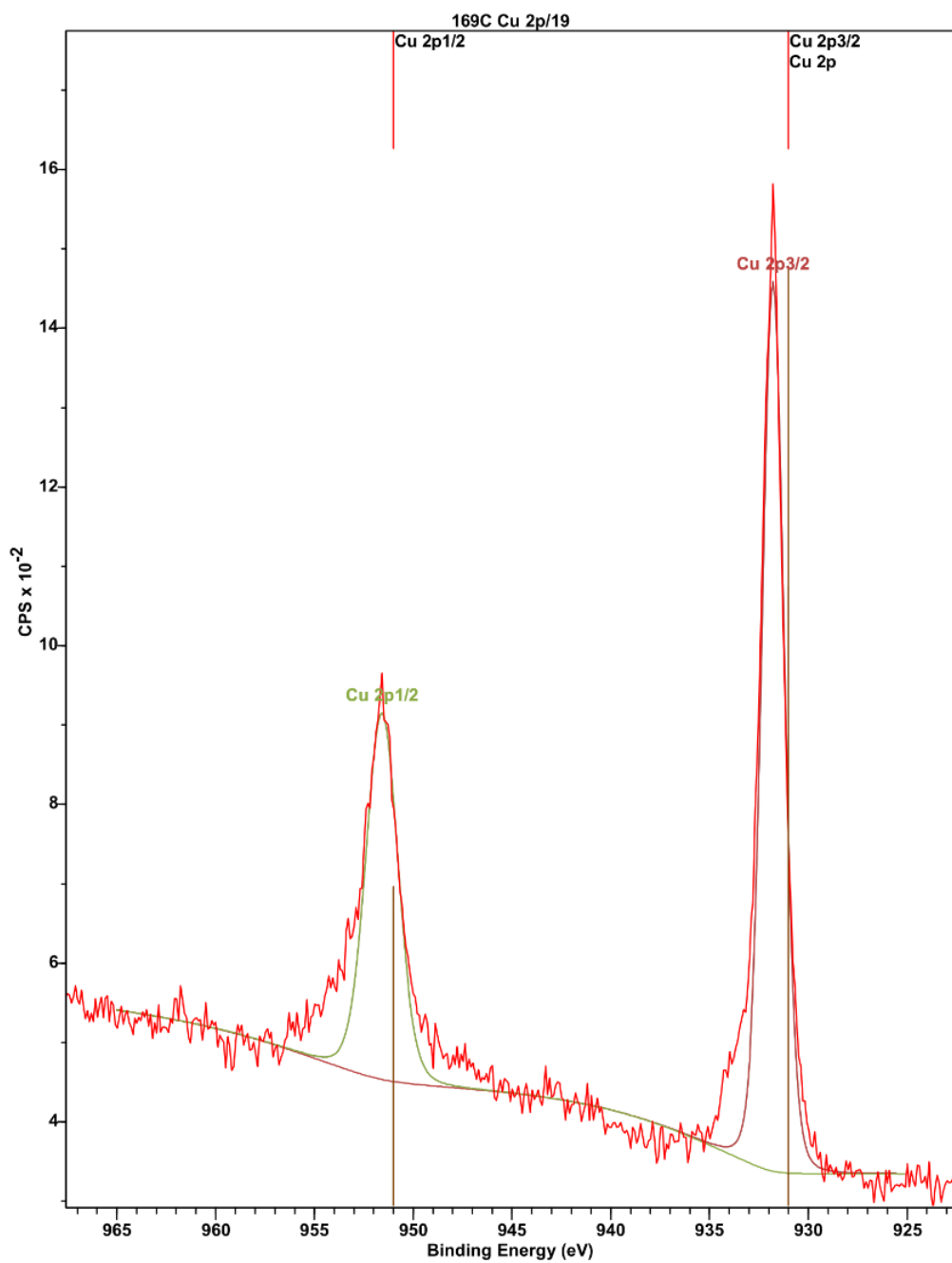


Figure S37: Cu 2p XPS region of **C**.

XPS data of **C** was processed and peak-fitted using CasaXPS. Peak fitting indicates the presence of only a single copper(I) environment, and is in agreement with all other structural characterization.

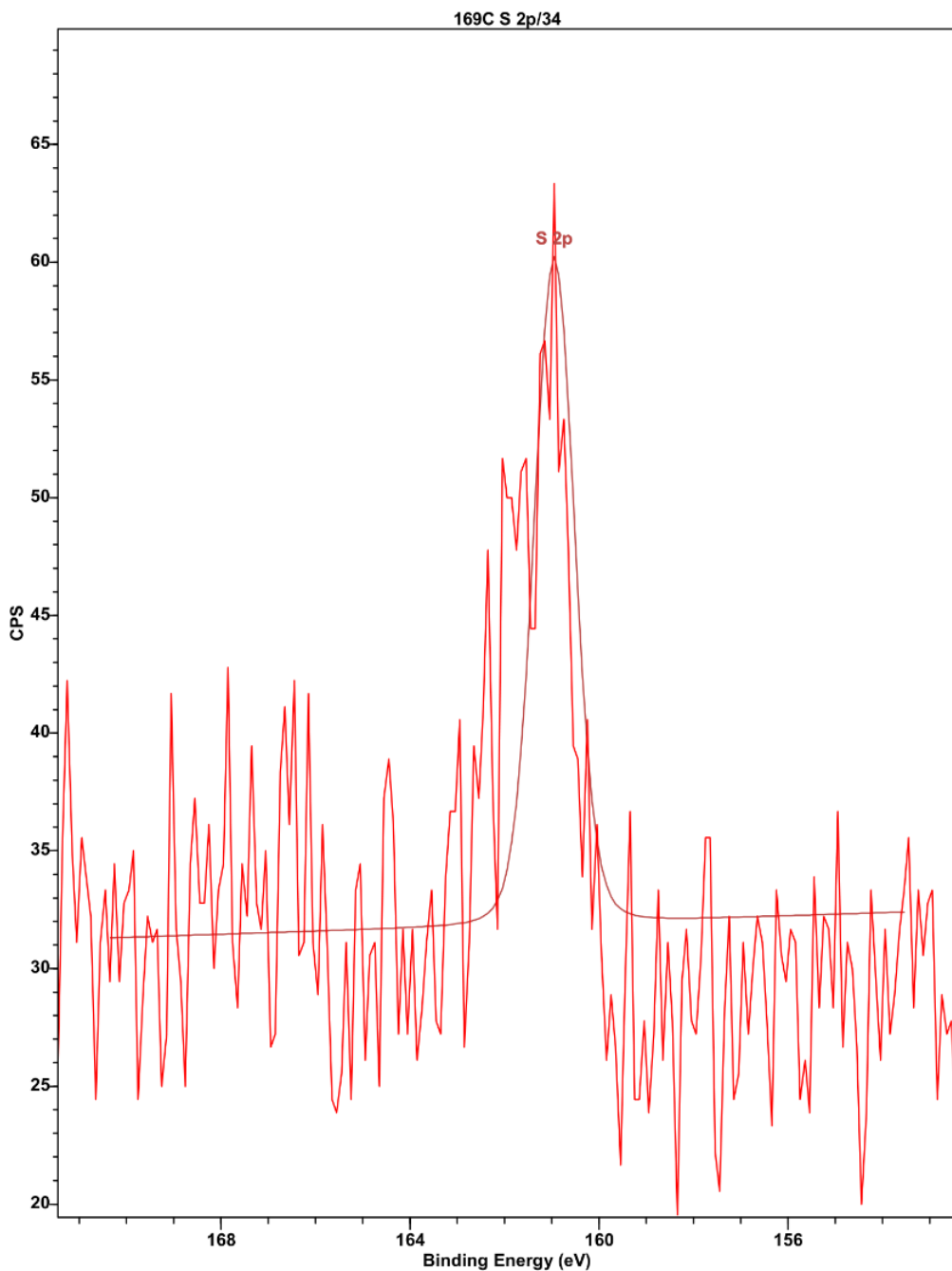


Figure S38: S 2p XPS region of C.

XPS data of C was processed and peak-fitted using CasaXPS. Peak fitting indicates the presence of only a single thiolate environment, and is in agreement with all other structural characterization. **Note:** The XPS instrument used to obtain measurements currently has decreased sensitivity in the S 2p region, resulting in lower signal to noise ratio.

f. Photophysical Measurements

Absorption and Emission Measurements

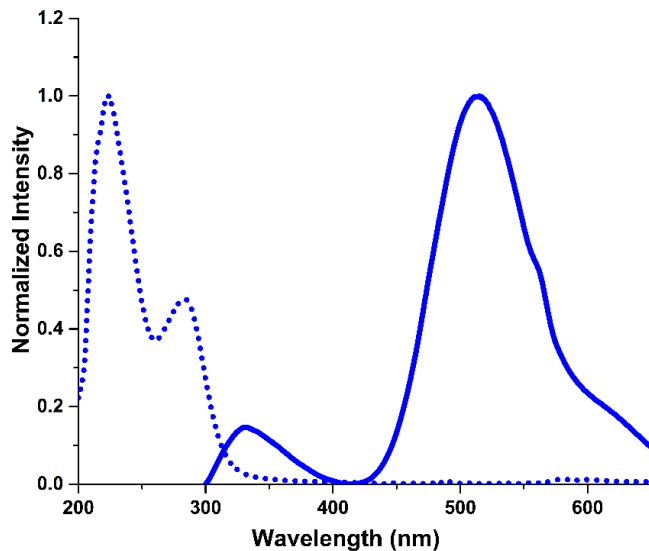


Figure S39: Absorption (dotted trace) and emission (solid trace) spectra of **C**.

Absorption (dotted trace) and emission (solid trace) of **C** have been normalized and plotted on the same set of axes. Both measurements were performed on suspension of **C** in *iso*-propanol. Emission spectrum was obtained by exciting the suspension with 280 nm light, and the emission was monitored between 300-650 nm. Although not as evident as in materials **A** and **B**, the artifact from the excitation wavelength (280 nm) is present as a slight shoulder at 560 nm.

Comparison of Emission Intensity at Different Excitation Wavelengths

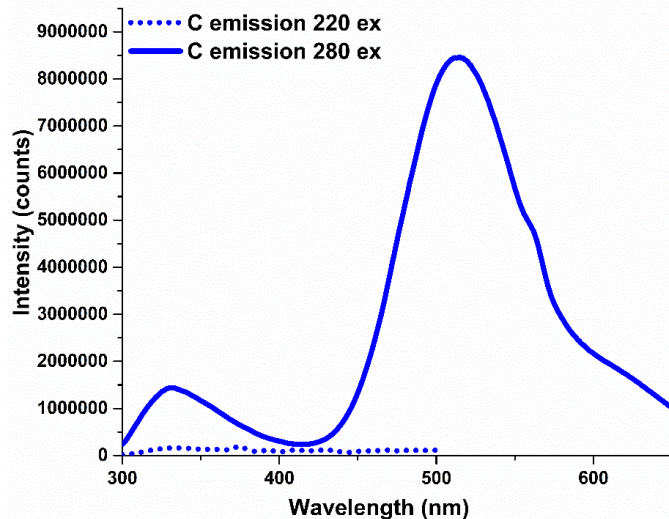


Figure S40: Comparison of emission intensity at different excitation wavelengths.

Emission traces when exciting a suspension of **C** in *iso*-propanol at 220 nm (dotted trace) and 280 nm (solid trace). Negligible emission can be correlated to excitation at 220 nm.

Quantum Yields

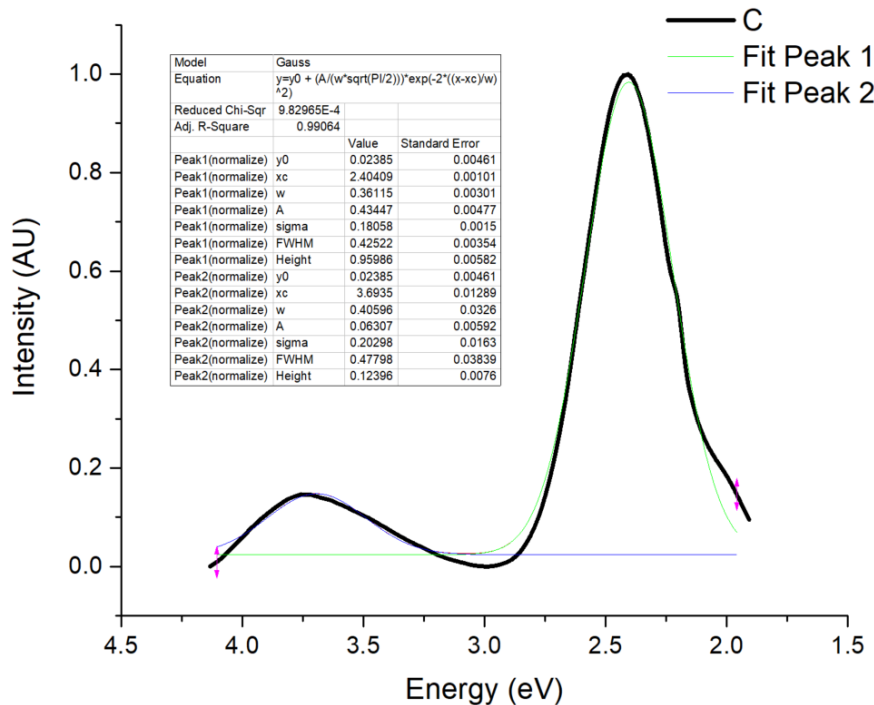


Figure S41: Peak fitting of C emission to determine the relative peak integrations of the high (12%) and low (87%) energy transitions

Lifetime Measurements

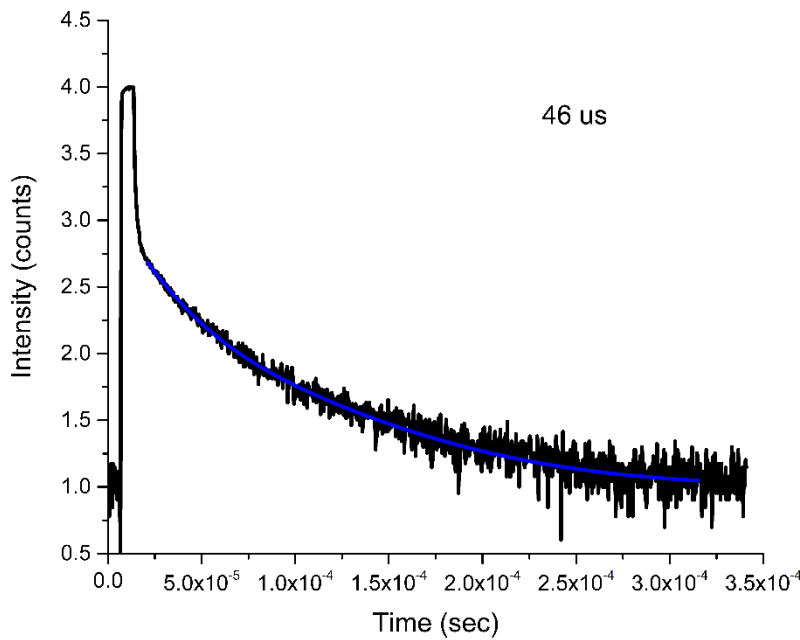


Figure S42: Lifetime plot of C, indicating a lifetime emission of 46 μ s.

g. Attempted MicroED

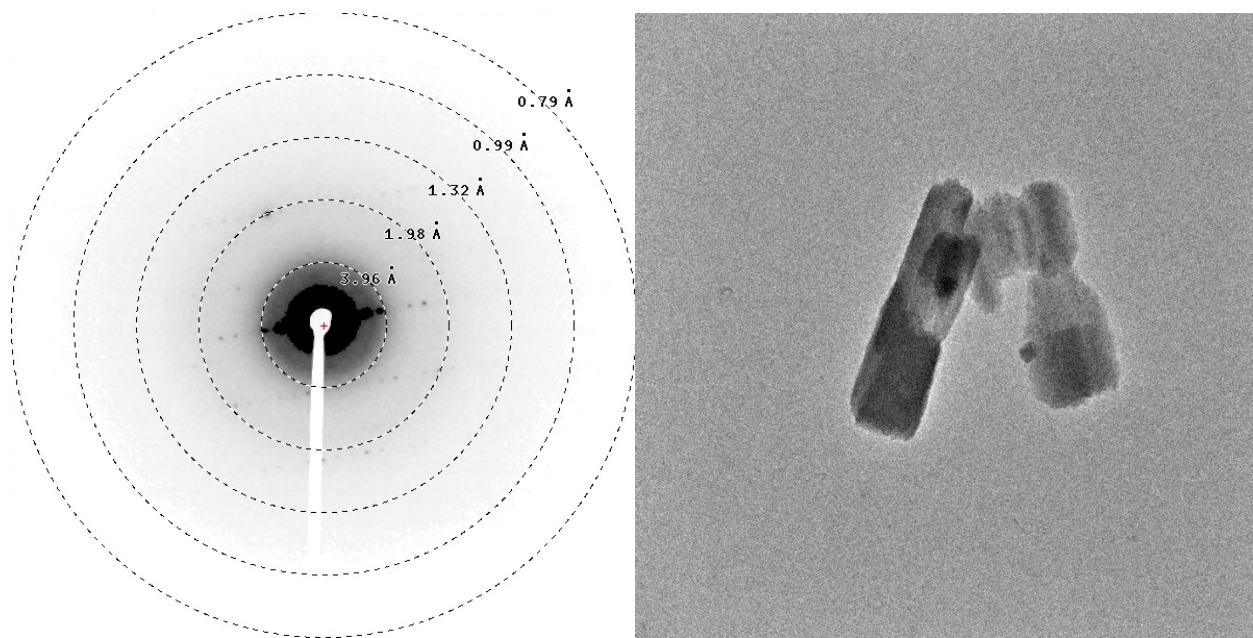


Figure S43: SAED and bright field image of C microcrystal on TEM grid.

MicroED was attempted using the previously described method outlined above. Selected Area Electron Diffraction (SAED, left image) confirmed the presence of crystalline material and several tilt series could be collected. Despite the single-crystalline nature of the sample, the highest resolution reflections were observed at $\sim 1.5 \text{ \AA}$, which is insufficient resolution for an *ab initio* solution. However, the obtained diffraction data could be indexed yielding approximate unit cell parameters of $a = 10.86$, $b = 18.71$, $c = 38.03$, $\alpha = 90$, $\beta = 90$, $\gamma = 90$ and a suggested space group of $P2_12_12_1$.

8. Supplementary Characterization and Data of D

a. Additional Electron Microscopy Images

Scanning Electron Microscopy

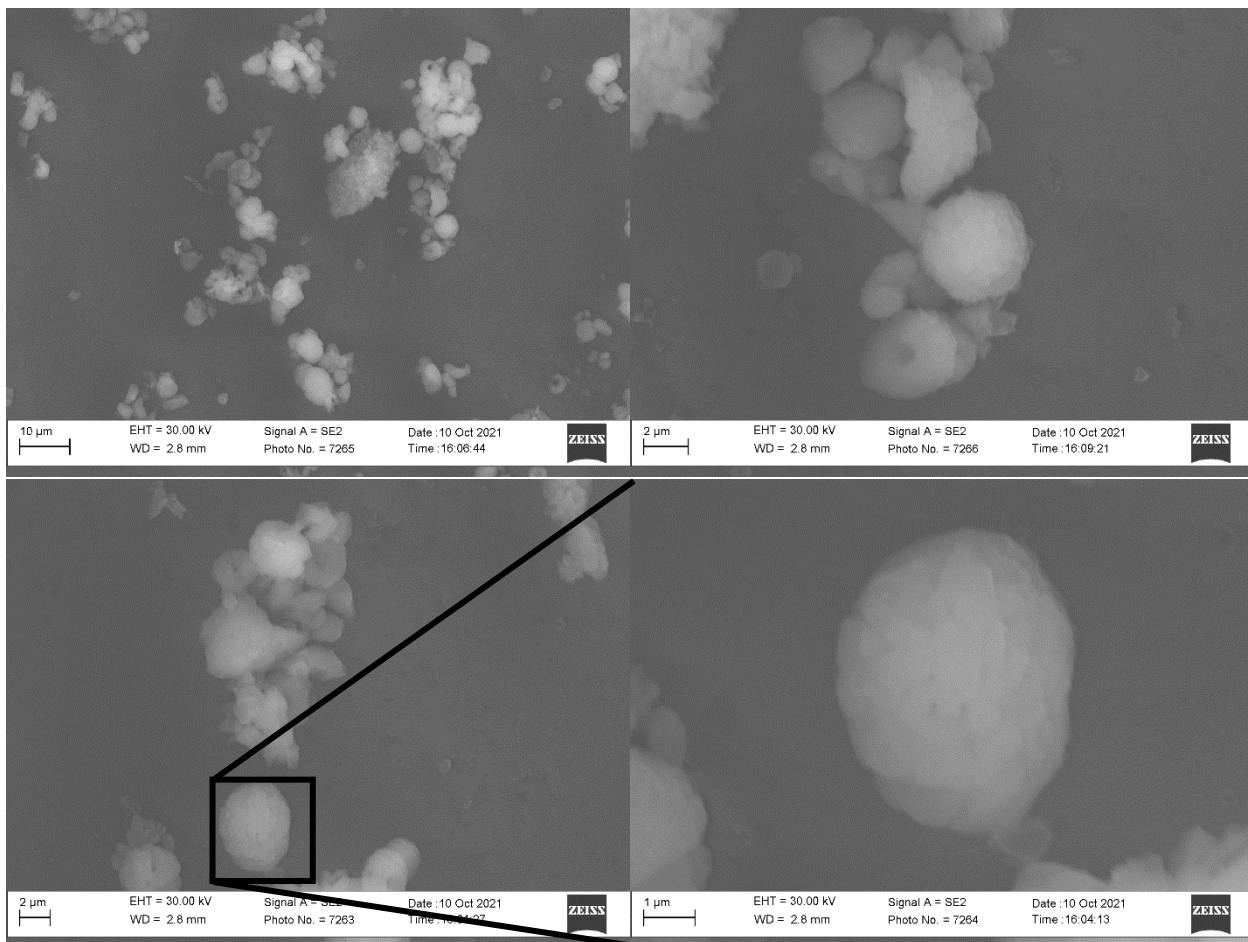


Figure S44: SEM images of D microcrystals deposited on a silicon wafer chip. SEM images reveal a microscale particle phase present in bulk D with an average particle size diameter of $3.47 \mu\text{m} \pm 0.72$. While spherical in nature, in higher magnification images (bottom right), the particles appear to be comprised of platelets stacked on top of one another. There is also some evidence of “donut-like” morphologies as seen in the top right SEM image.

Transmission Electron Microscopy

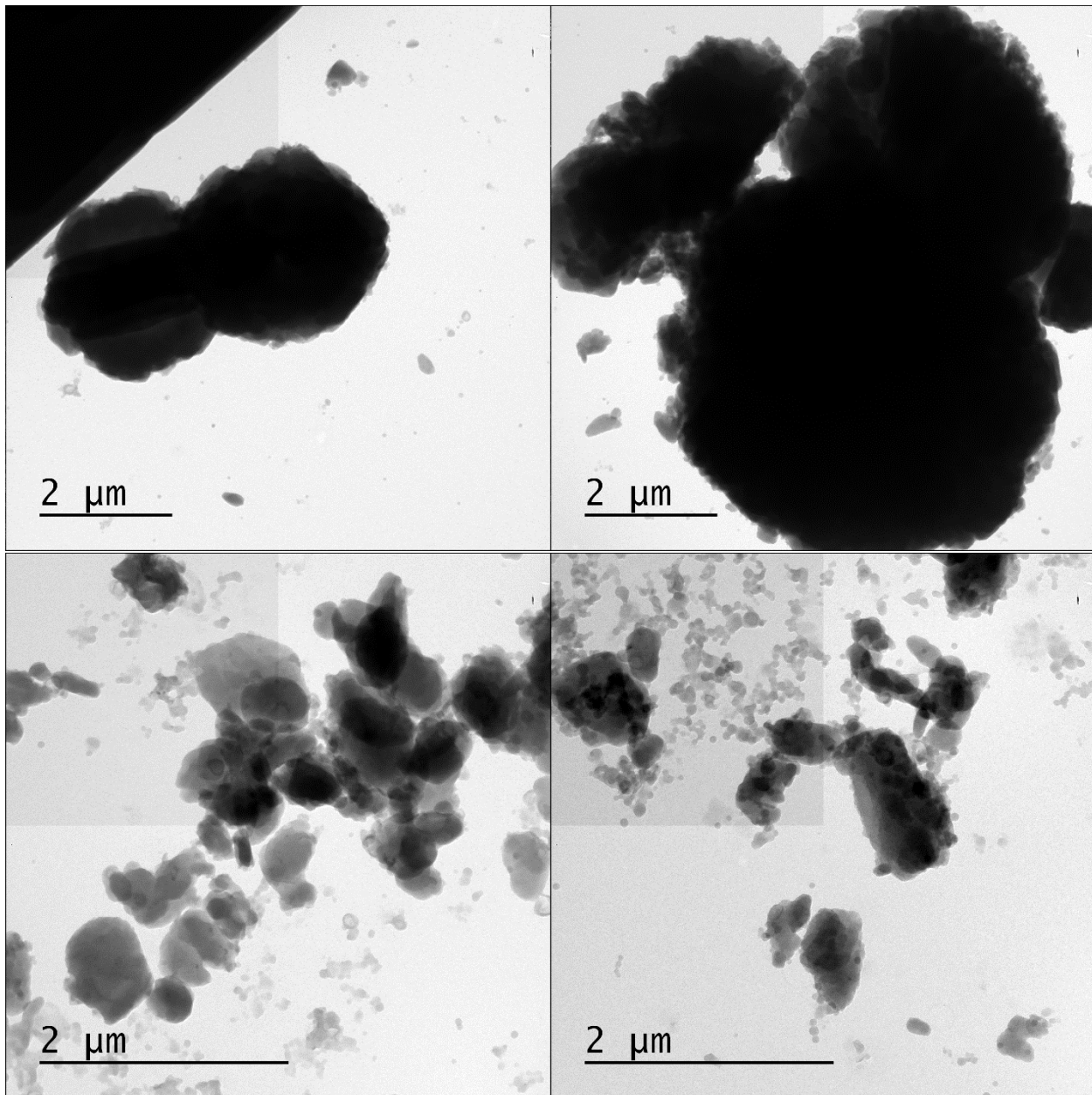


Figure S45: TEM images of **D** microcrystals deposited a copper grid (200 mesh, Formvar/Carbon or Carbon Film only). TEM images of **D** reveal the presence of spherical nanoparticles comingled with the larger aggregates observed by SEM, though significantly less prominent than in **B**.

b. Powder X-ray Diffraction Pattern

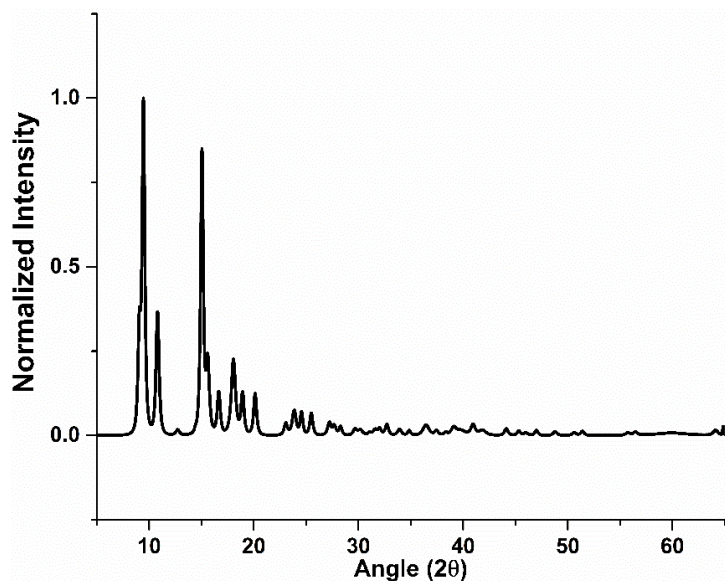


Figure S46: Powder X-ray diffraction pattern of **D** microcrystals deposited on a zero-background plate. Sample was diffracted from 5.000° to 65.000° with a step size of 0.016° . See included spreadsheet for peak list and corresponding intensities.

c. Infrared Spectroscopy

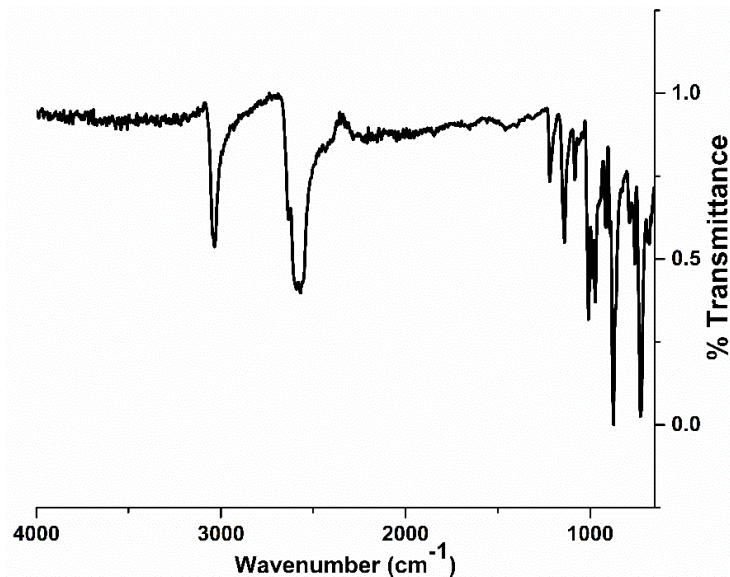


Figure S47: FTIR spectrum of **D**.

FTIR spectrum of **D** reveals no signals that could be correlated to residual starting material (CuOAC (C=O : $\sim 1500\text{ cm}^{-1}$), HS-oCB (H-Se: $\sim 2500\text{ cm}^{-1}$), *iso*-propanol (H-C: $\sim 3000\text{ cm}^{-1}$; H-O: $\sim 3500\text{ cm}^{-1}$)). Two diagnostic resonances attributed to the carborane cluster (H-C_{carborane}: 3000 cm^{-1} ; H-B_{carborane}: 2500 cm^{-1}) are present and are expected to be slightly asymmetric as a function of the *ortho*-carboranyl-selenolate asymmetry.

d. Thermogravimetric Analysis

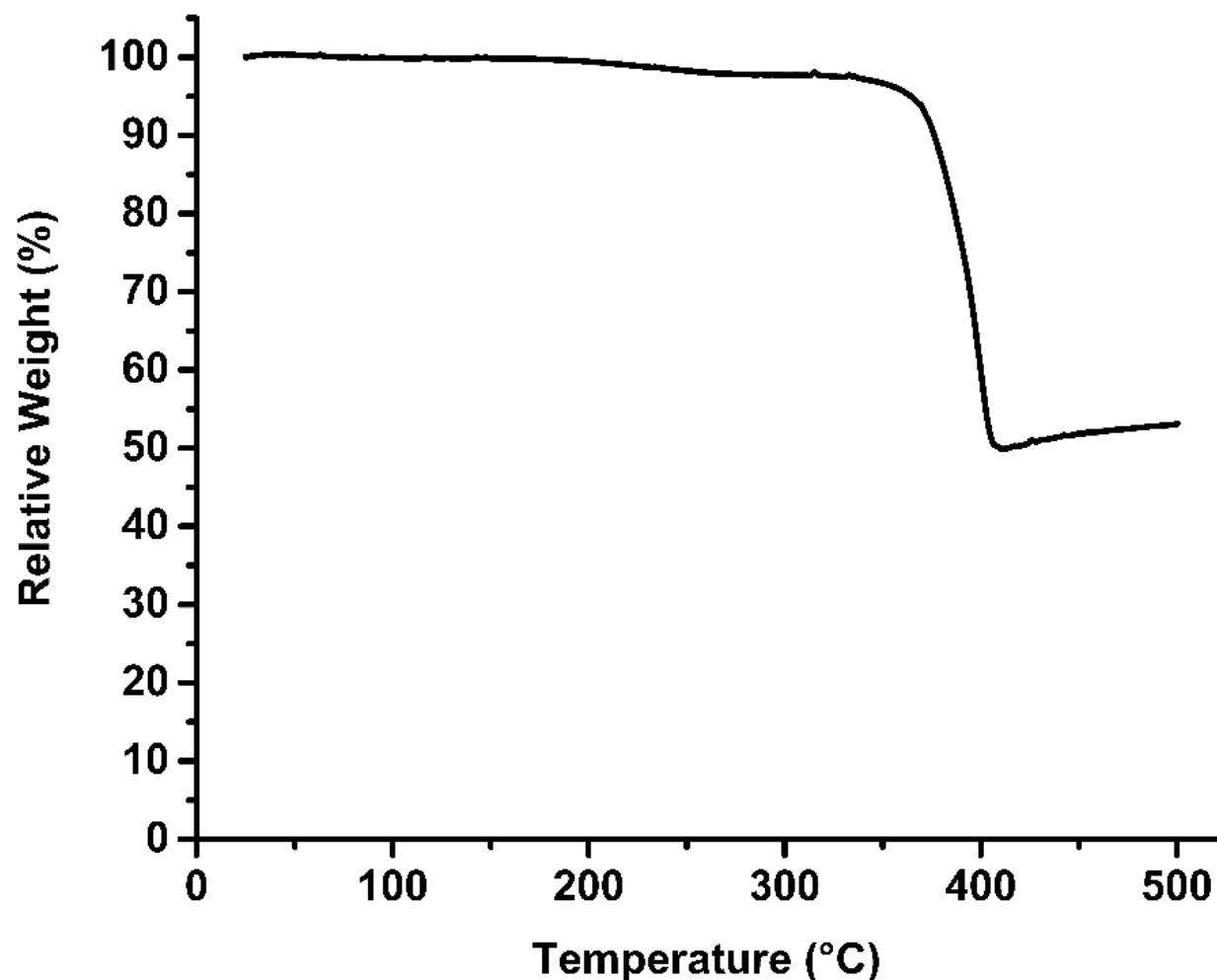


Figure S48: TGA of **D**.

TGA of **D** indicates the material is thermally stable until 375 °C, after which, the material decomposes until reaching 50% relative weight at 400 °C. There is no evident desolvation step that would indicate the presence of solvent adducts within the material, which would be expected near 100 °C.

e. X-ray Photoelectron Spectroscopy

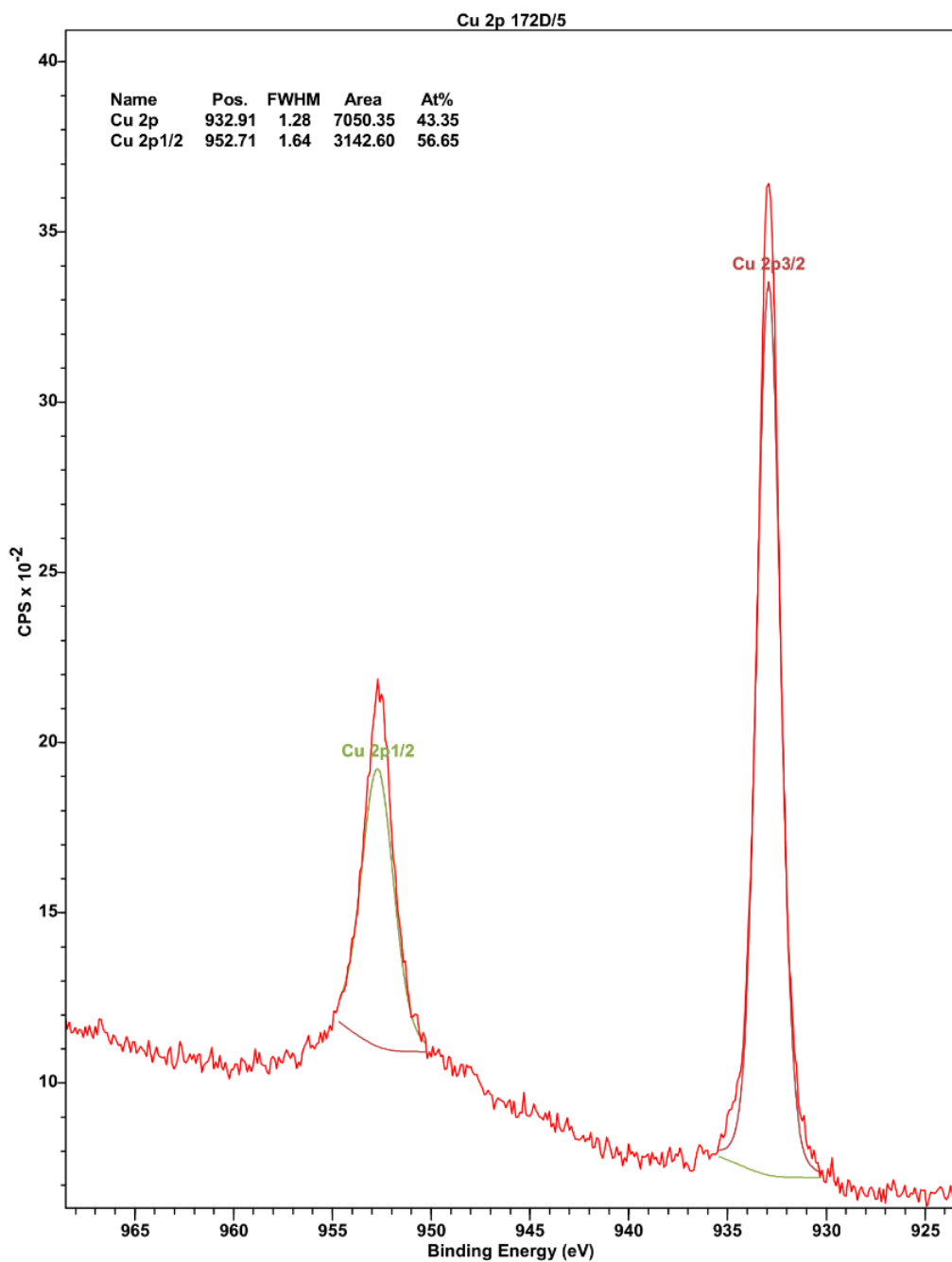


Figure S49: Cu 2p XPS region of **D**.

XPS data of **D** was processed and peak-fitted using CasaXPS. Peak fitting indicates the presence of only a single copper(I) environment, and is in agreement with all other structural characterization.

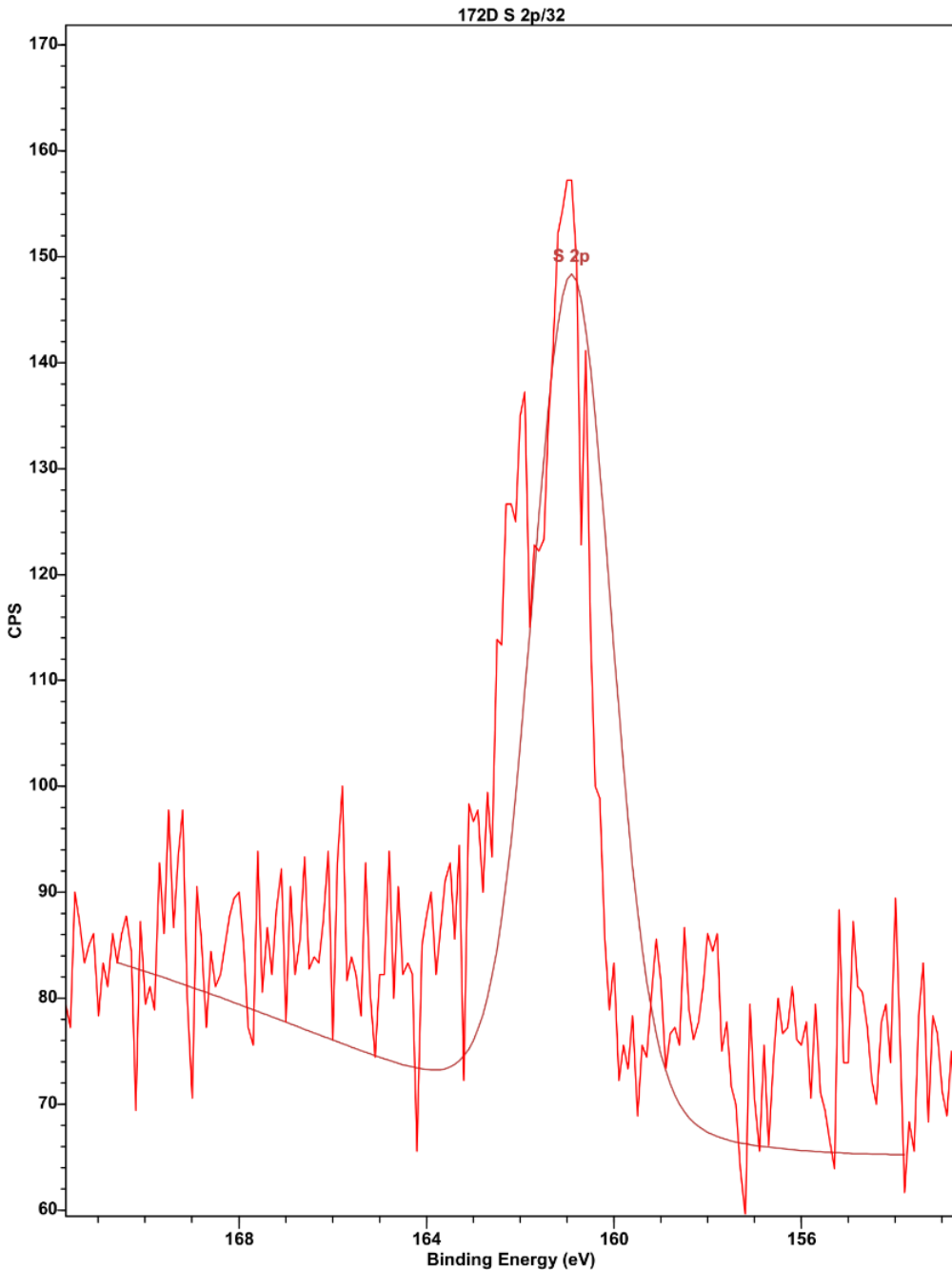


Figure S50: S 2p XPS region of **D**.

XPS data of **D** was processed and peak-fitted using CasaXPS. Peak fitting indicates the presence of only a single thiolate environment, and is in agreement with all other structural characterization. **Note:** The XPS instrument used to obtain measurements currently has decreased sensitivity in the S 2p region, resulting in lower signal to noise ratio.

f. Photophysical Measurements

Absorption and Emission Measurements

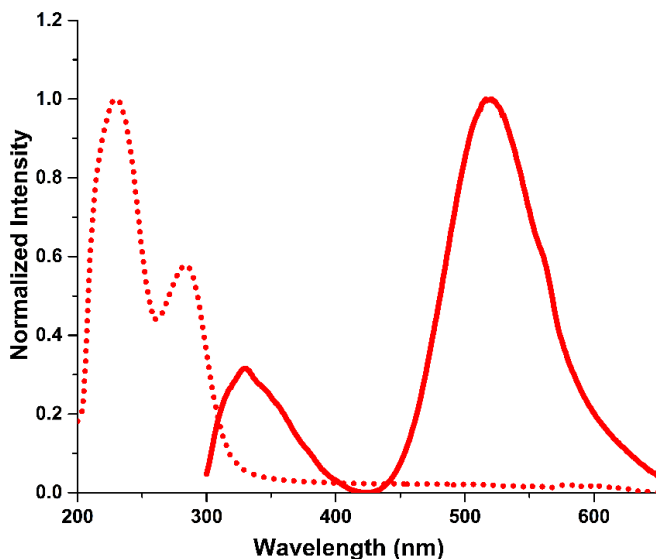


Figure S51: Absorption (dotted trace) and emission (solid trace) spectra of **D**.

Absorption (dotted trace) and emission (solid trace) of **D** have been normalized and plotted on the same set of axes. Both measurements were performed on suspension of **D** in *iso*-propanol. Emission spectrum was obtained by exciting the suspension with 280 nm light, and the emission was monitored between 300-650 nm. Although not as evident as in materials **A** and **B**, the artifact from the excitation wavelength (280 nm) is present as a slight shoulder at 560 nm.

Comparison of Emission Intensity at Different Excitation Wavelengths

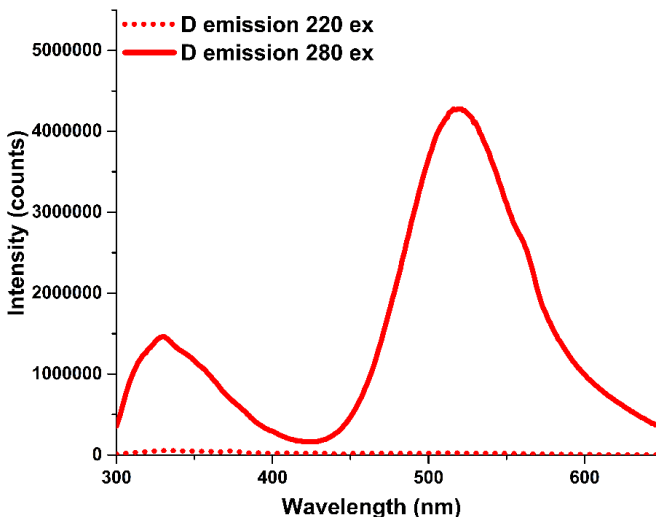


Figure S52: Comparison of emission intensity at different excitation wavelengths.

Emission traces when exciting a suspension of **D** in *iso*-propanol at 220 nm (dotted trace) and 280 nm (solid trace). Negligible emission can be correlated to excitation at 220 nm.

Quantum Yields

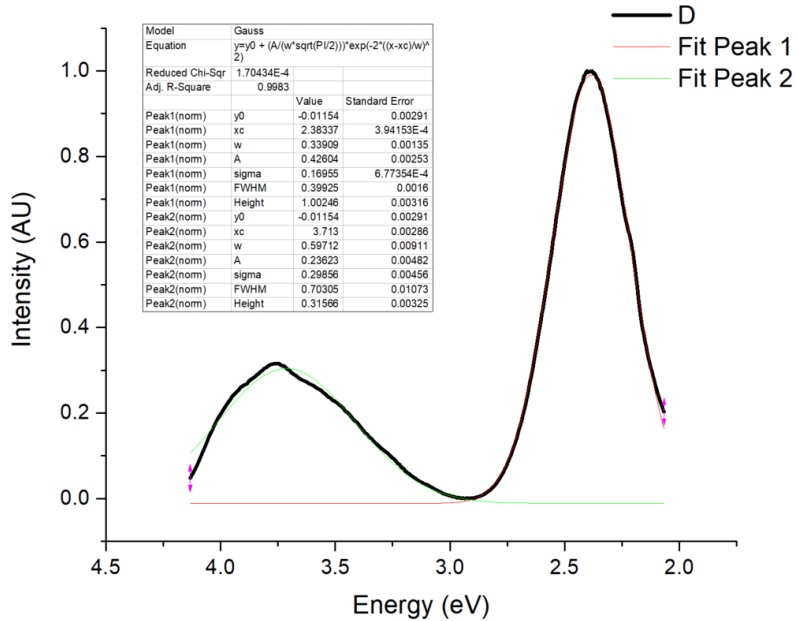


Figure S53: Peak fitting of **D** emission to determine the relative peak integrations of the high (36%) and low (64%) energy transitions

Lifetime Measurements

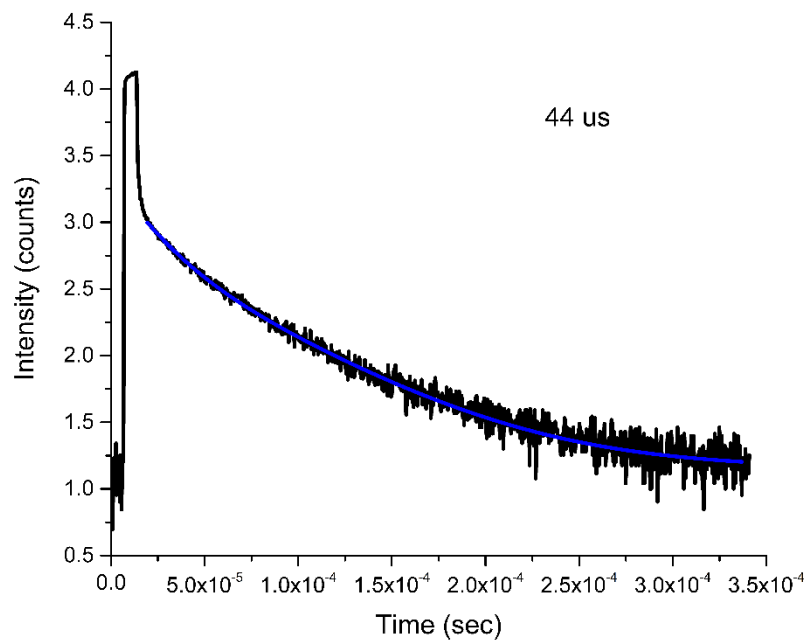


Figure S54: Lifetime plot of **D**, indicating a lifetime emission of 44 μ s.

9. Further Analysis of Literature Copper Selenide Clusters

To further understand the Cu-Se bonding arrangement, a search of the CCDC was performed, targeting the isolated Cu_4Se_4 observed by MicroED. Using ConQuest 2.0.4, a build query was developed using the below search parameters:

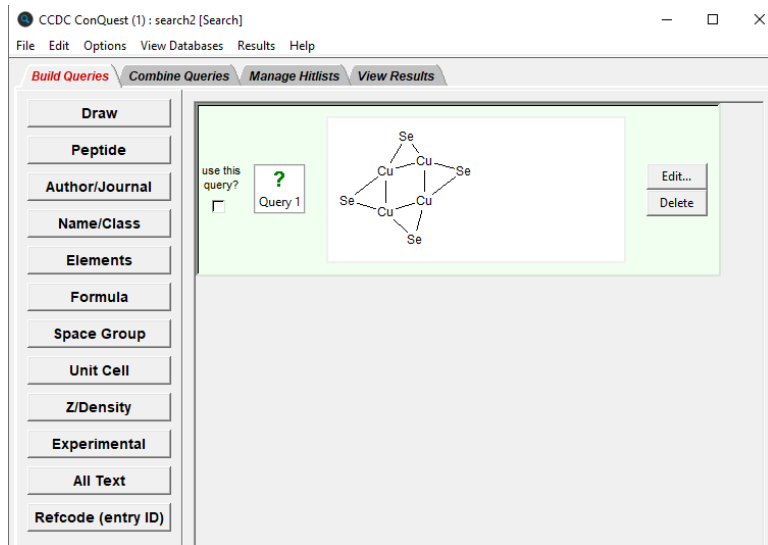


Figure S55: CCDC ConQuest search window with Cu_4Se_4 bonding arrangement searched for.

Searching for this bonding arrangement yielded 39 results of crystallographically characterized Cu_4Se_4 bonding units, see below for tabulated RefCodes for each entry.

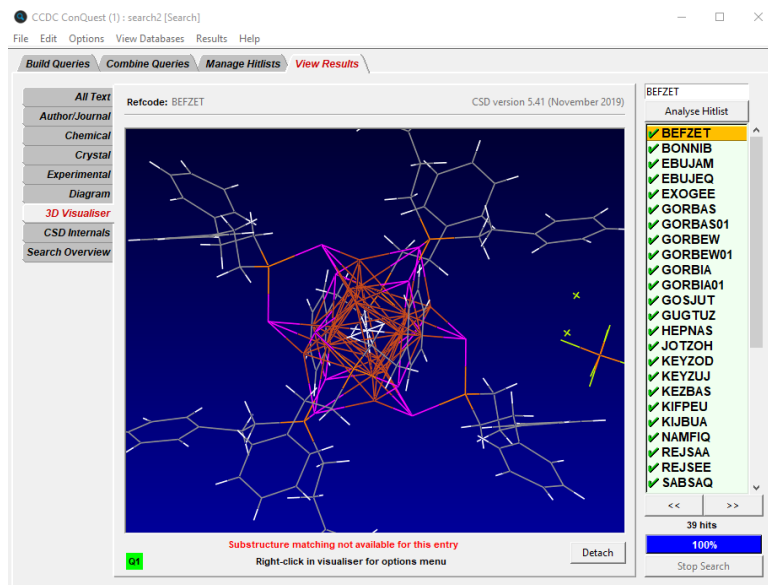


Figure S56: ConQuest search result window.

BEFZET	BONNIB	EBUJAM	EBUJEQ	EXOGEE	GORBAS	GORBAS01	GORBEW
GORBEW01	GORBIA	GORBIA01	GOSJUT	GUGTUZ	HEPNAS	JOTZOH	KEYZOD
KEYZUJ	KEZBAS	KIFPEU	KIBJUA	NAMFIQ	REJSAA	REJSEE	SABSAQ
TAMYEL	TUNBIP	VEYROH	VEYRUN	WESQIV	WESQOB	WIXDUF	XAHMAU
XAHAMAU01	XAHMEY	XAHMEY01	XAJGIZ	XUBKUA	XUBLAH	YUKBEL	

Surprisingly, over half (21) of the entries consist of larger copper-selenide clusters with complex Cu-Cu and Cu-Se bonding arrangements. Meanwhile, some smaller, molecular, clusters have been crystallographically characterized and contain more analogous Cu₄Se₄ bonding arrangements to that found in A. A few selected examples have been rendered below accompanied by their RefCode (atoms comprising the ligands, other than the carbon atom bound to the selenolate have been hidden for clarity).

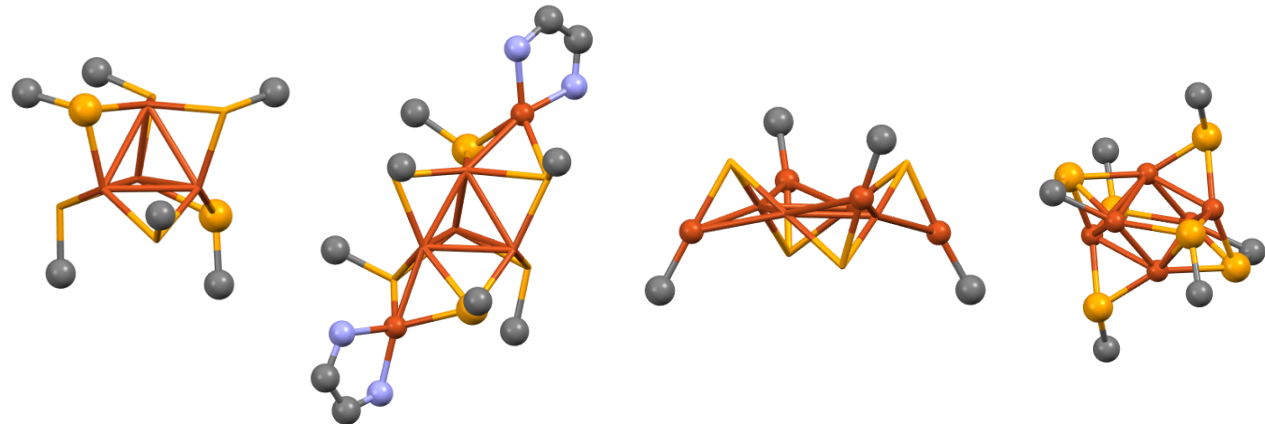


Figure S57: RefCodes (left to right): BONNIB, GUGTUZ, WIXDUF, YUKBEL

Of the smaller clusters, the vast majority contain tetrahedral copper tetramers (see BONNIB, GUGTUZ, YUKBEL) with only one example (WIXDUF, reference 12) somewhat resembling the observed Cu₄Se₄ in material A with some notable differences. Unlike in A, there are no ligands attached to the selenolate and the cluster is instead structured by N-heterocyclic carbenes bound to the peripheral copper atoms (see below). Furthermore, the cluster in WIXDUF is substantial larger with an overall molecular formula of Cu₈Se₄.

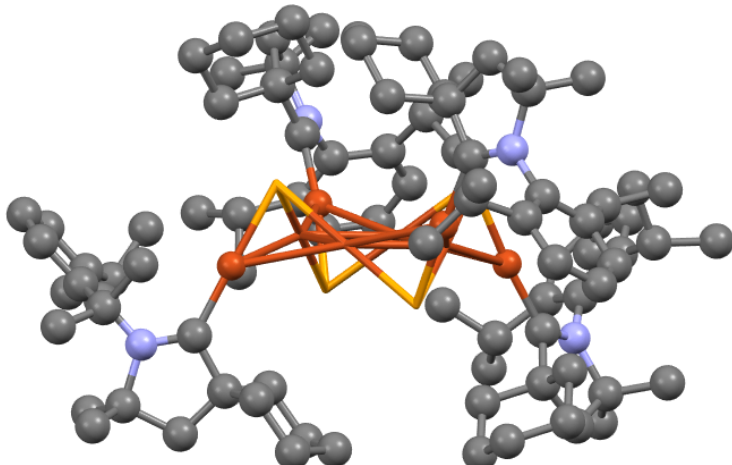


Figure S58: Single crystal X-ray structure of WIXDUF.

10. ^1H and ^{11}B NMR Experiments of Dissolved Materials A-D

As a further assessment of both purity from starting materials (chalcogenols, *iso*-propanol) in addition to understanding potential intermolecular forces between the copper chalcogenides clusters. Approximately 10 mg of each material was added to an NMR tube and dissolved in 0.4 mL of CD_2Cl_2 . Unexpectedly, the materials appear to be only partially soluble in dichloromethane, particularly those containing *ortho*-carborane (see right, samples are **A**, **B**, **C**, **D** from left to right).

In contrast to the purity of the materials suggested by TGA, ^1H NMR of **A-D** suggested the presence of up to 20% *iso*-propanol. This apparent impurity is likely inflated from the real purity due to the poor solubility of materials **B** and **D**, and should be more closely associated with the lack of solvent adducts observed by TGA. In all ^1H NMRs (see below), no chalcogenol resonance is observed.



Figure S59: NMR samples of **A-D**

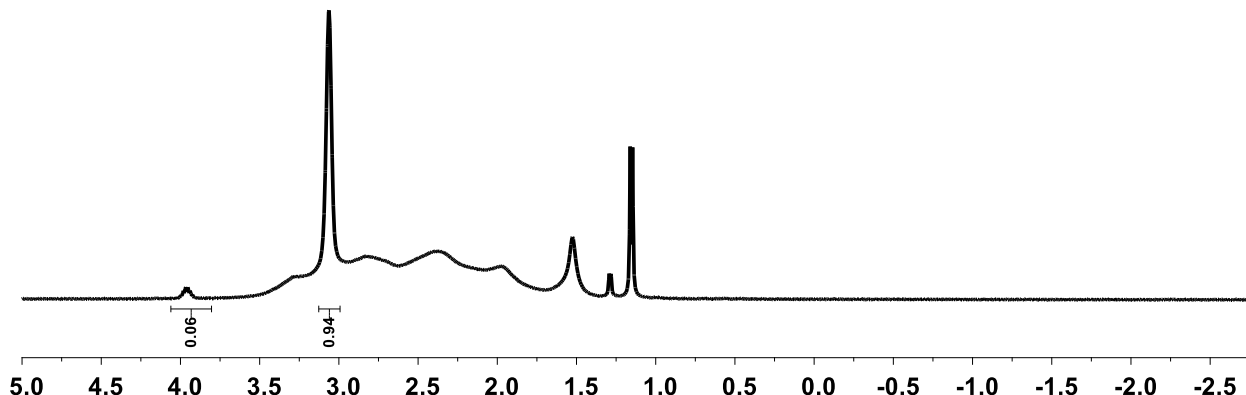


Figure S60: ^1H NMR of **A**

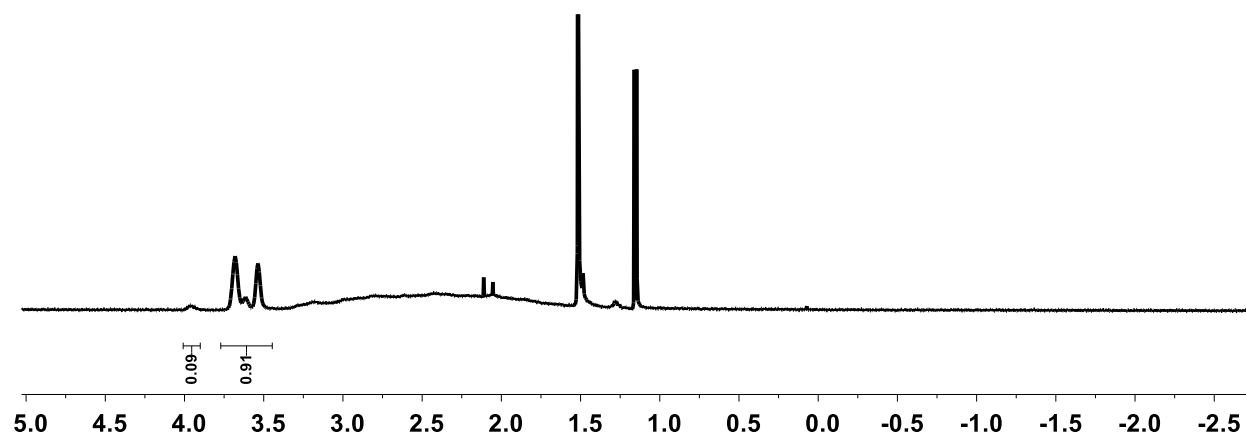


Figure S61: ^1H NMR of **B**

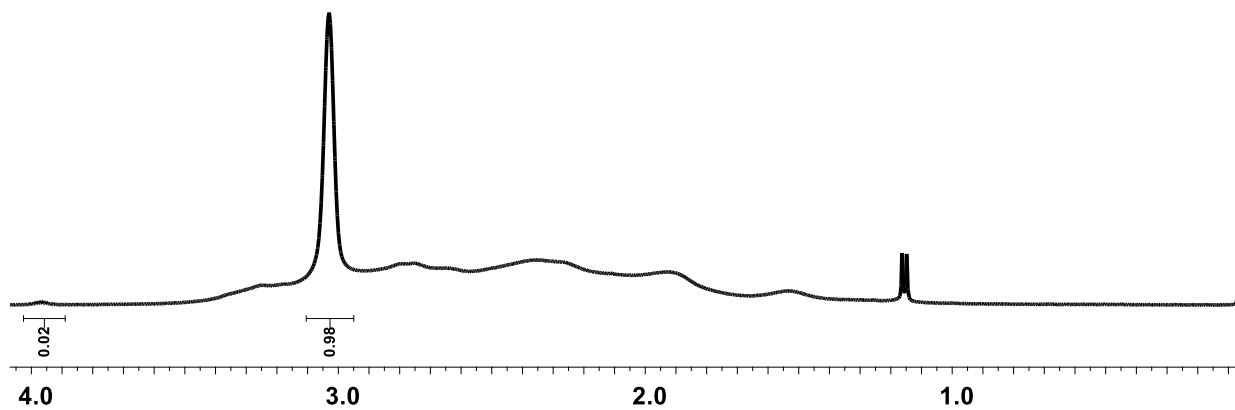


Figure S62: ^1H NMR of **C**

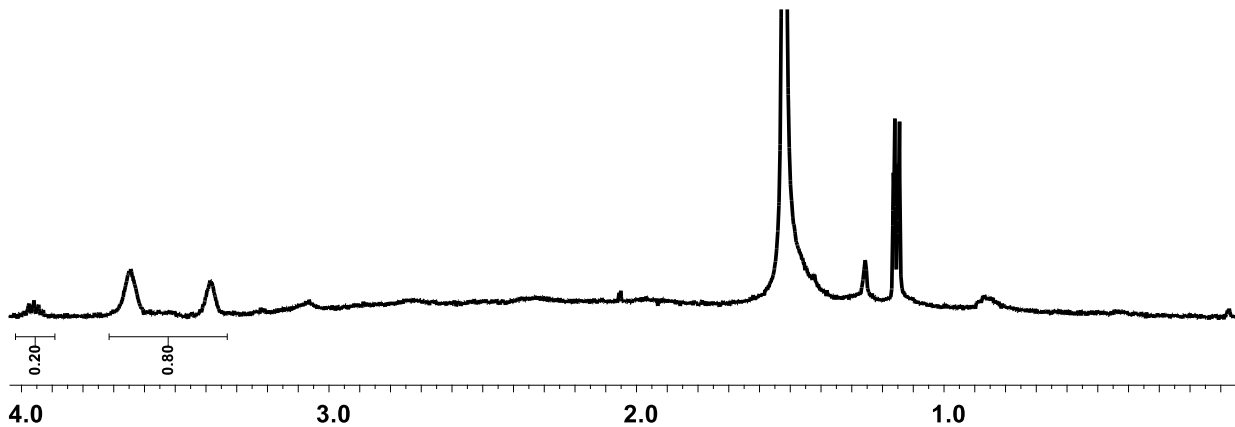


Figure S63: ^1H NMR of **D**

^{11}B NMR spectroscopy of materials **A-D** further corroborated the observations made by FTIR spectroscopy (see below). The NMR spectra indicate that the boron cluster cage is fully intact with no decomposition of the cluster observed. As expected, there are slight shifts in the ^{11}B NMR resonances attributed to the boron nucleus bound to the exopolyhedral chalcogen-based substituent (Se, S). More noticeably, however, is the significant broadening of the ^{11}B NMR resonance assigned to the B(3) boron vertex in a position distal to the exopolyhedral boron-chalcogen bond. While this is difficult to see in materials **B** and **D** due to overlapping resonances in the upfield region, it is quite prominent in materials **A** and **C**. This broadening is likely attributed to the rotation of the carborane cage relative to the exopolyhedral B-Se or B-S bond while the copper cluster is dissolved in solution.

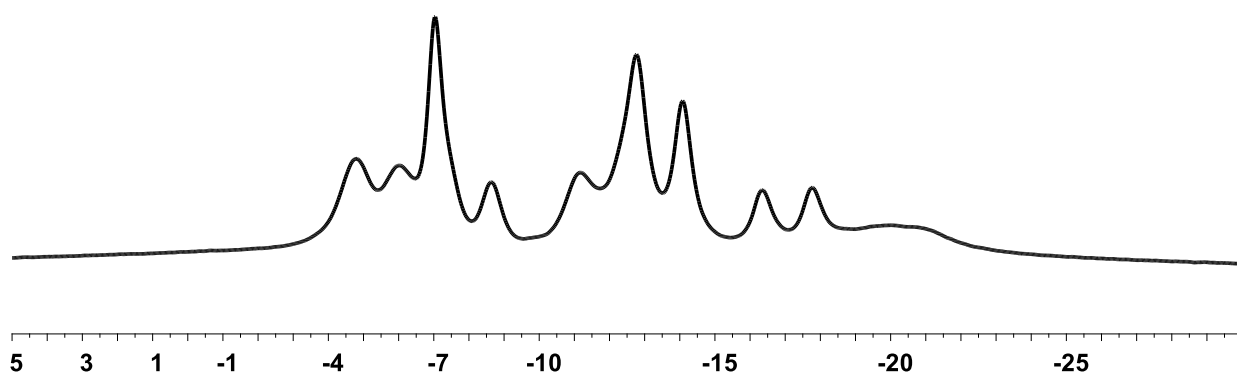


Figure S64: ^{11}B NMR of **A**

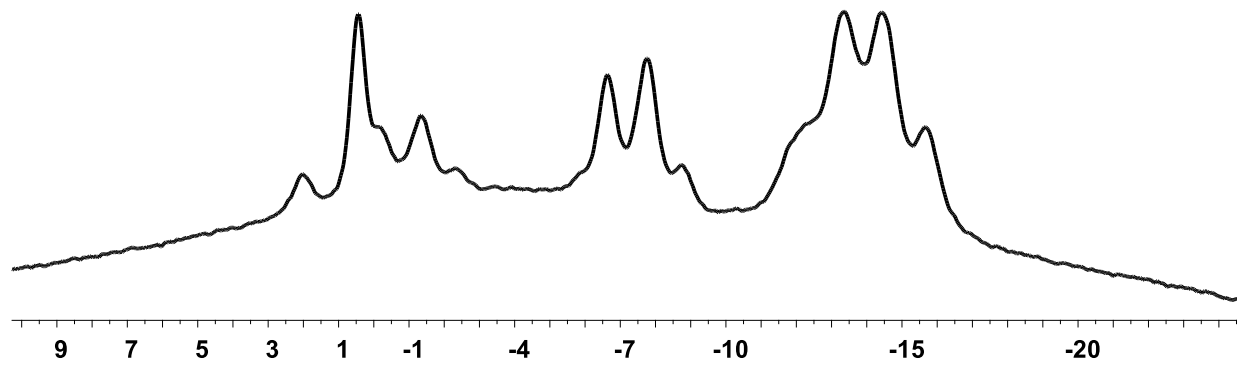


Figure S65: ^{11}B NMR of **B**

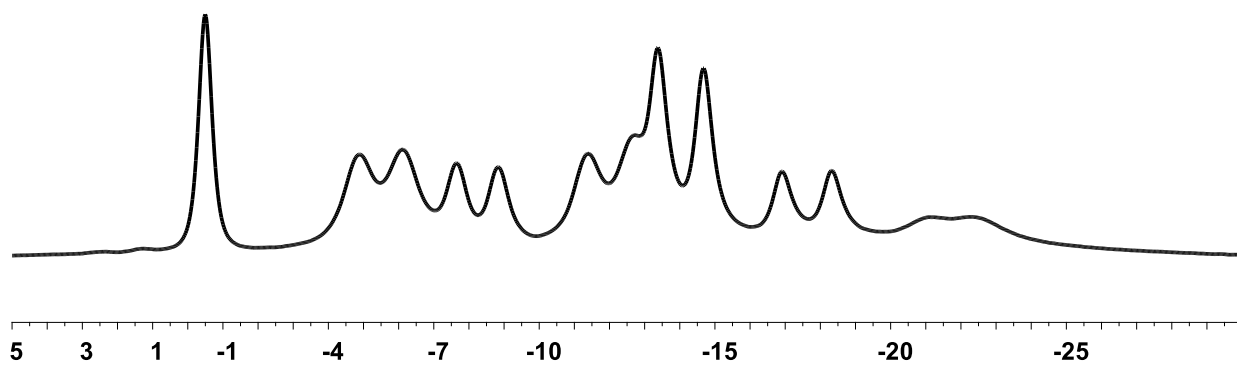


Figure S66: ^{11}B NMR of **C**

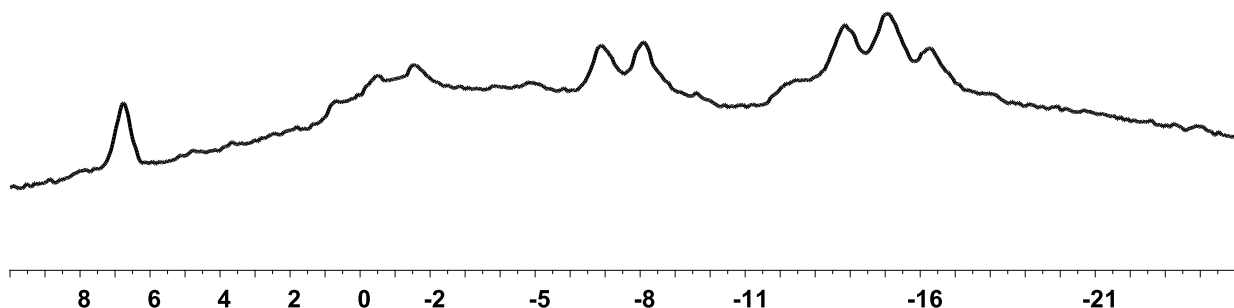


Figure S67: ^{11}B NMR of **D**

11. Study and Comparison of Literature PXRD Patterns with Varying Carborane Isomers and Chalcogens

To validate the observed differences in the PXRD patterns of materials **A** and **B**, **B** and **C**, and **C** and **D**, the comparison of simulated PXRD patterns of molecular carborane-based compounds with different carborane isomers and chalcogens was performed (references 9 and 13).

Comparison of Simulated PXRD for 9-TEMPO-*Ortho*-Carborane (9-TEMPO-oCB) and 9-TEMPO-*Meta*-Carborane (9-TEMPO-mCB)

Similar to the observed differences in the PXRD peaks between materials **A** and **B**, or **C** and **D**, minor deviations are expected as a result of different molecular packing in the solid state as a result of the carborane dipole. Below you will find the simulated PXRD peak patterns of 9-TEMPO-*ortho*-carborane (9-TEMPO-oCB, green) and 9-TEMPO-*meta*-carborane (9-TEMPO-mCB, black). Despite the molecular similarity between the two TEMPO adducts, the two PXRD patterns show differences on a similar magnitude as seen when comparing the PXRD patterns of materials containing separate carborane isomers.

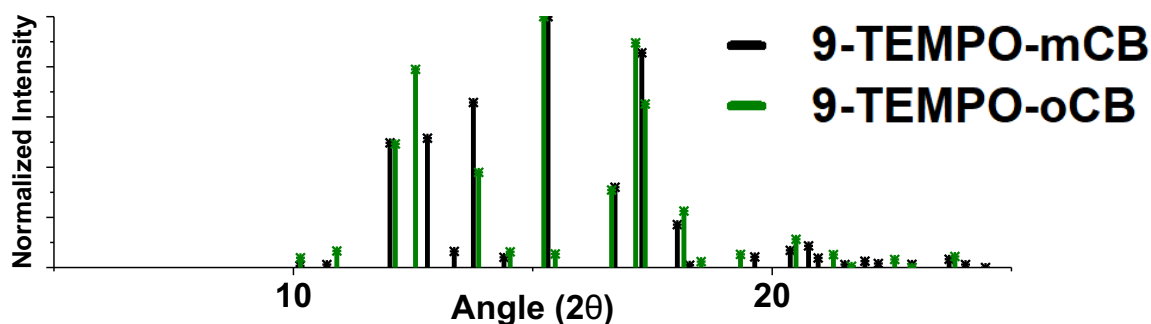


Figure S68: Overlay of calculated PXRD patterns of 9-TEMPO-mCB (black) and 9-TEMPO-oCB (green)

Comparison of Simulated PXRD for *Meta*-Carborane Diselenide ($(\text{Se-mCB})_2$) and Ditelluride ($(\text{Te-mCB})_2$)

Similar to the observed differences in the PXRD peaks between materials **A** and **C**, or **B** and **D**, minor deviations are expected as a result of the presence of differently sized chalcogens present in the material. Below you will find the simulated PXRD peak patterns of *meta*-carborane diselenide ($(\text{Se-mCB})_2$, black) and *meta*-carborane ditelluride ($(\text{Te-mCB})_2$, green). As expected, by increasing the size of the chalcogen present in the crystal, a general shift to lower 2theta values is observed. This trend is also evident when comparing the PXRD patterns of material **A** and **C**, or **B** and **D**.

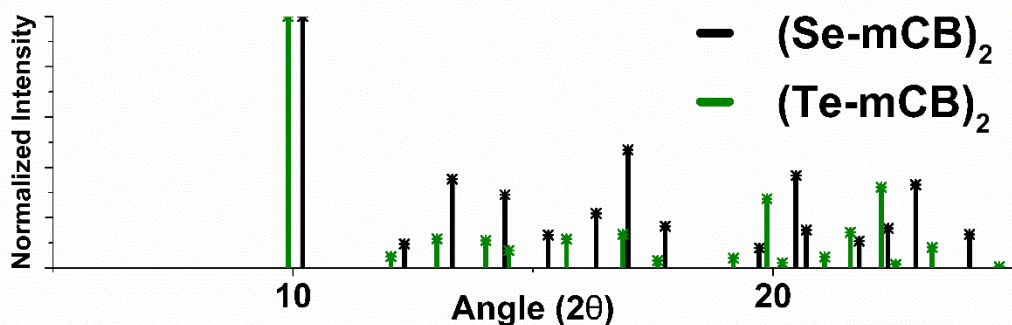


Figure S69: Overlay of calculated PXRD patterns of $(\text{Se-mCB})_2$ (black) and $(\text{Te-mCB})_2$ (green)

12. Qualitative Assessment of Emission Properties in Various Solvents and Media

To further understand the emission properties and mechanism at play in materials **A-D** the emission of materials **A** and **B** were qualitatively assessed in several solvents and media.

Emission of Soluble Solutions of A and B in Organic Solvents

Surprisingly, all materials are partially soluble in several polar, aprotic organic solvents, and all emissive properties are no longer present after dissolution at room temperature (see below). Unexpectedly, the solubility of **B** in dichloromethane is significantly lower than that of **A**. This is likely a result of the stronger intermolecular forces present in the *ortho*-carborane-containing material hindering dissolution. Upon freezing the solutions of **A** and **B** to 77 K in liquid nitrogen, emission of the copper chalcogenide clusters in all cases return, albeit significantly red-shifted relative to the room temperature emission from the microcrystals as obtained from the reaction mixture (see below). This suggests that emission from the copper chalcogenide clusters occurs only when molecular movements are decreased either through decreasing the temperature of the molecule, as is the case in the below organic solutions, or by enforcing the clusters into a crystalline lattice, where motion would be limited by intermolecular interactions between adjacent clusters.

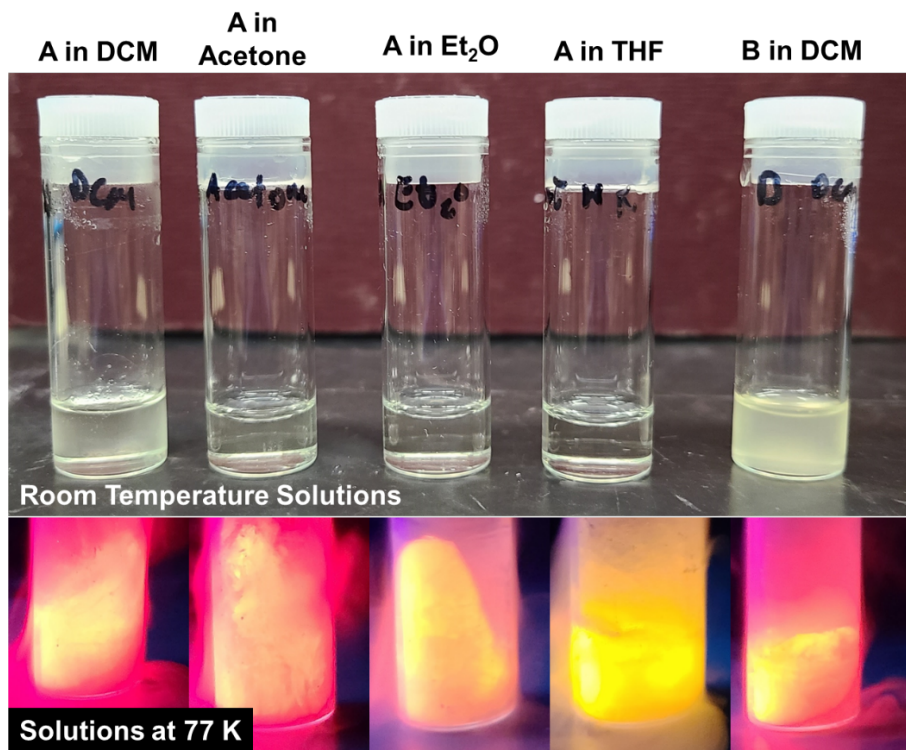


Figure S70: Images of dissolved **A** and **B** in several solvents exhibiting emission at 77 K.

To confirm that the copper selenide clusters were still intact for material **A**, the dichloromethane solution was triturated with pentane, and the acetone solution was layered with *iso*-propanol. In both cases, **A** precipitated, and the initial green emission of the as synthesized microcrystals returned (see below).

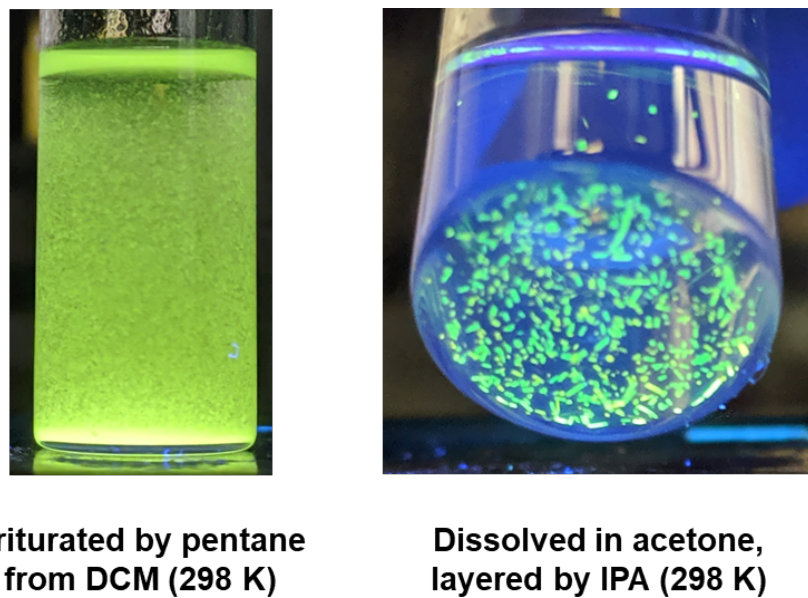


Figure S71: Emission of triturated (left) and recrystallized (right) **A** at room temperature.

Emission of A in Polymer Films

In addition to restricting molecular movement in the excited state by either freezing or crystallizing the copper selenide clusters, movement can also be restricted by a polymer matrix. In this situation, molecular movement would theoretically be limited by intermolecular interactions between the polymer matrix and copper selenide cluster, conceptually similar to crystallization. Solutions of PMMA (top) and polystyrene (bottom) were prepared in dichloromethane before the addition of several milligrams of A. Once fully dissolved, the solutions were cast onto quartz plates. Surprisingly, the as cast films exhibited similar luminescence to the frozen solutions though were still red-shifted relative to the pristine crystals (see below). This suggests that molecular movement is in fact somewhat limited while in the polymer matrix, but still less of that when in a crystalline matrix.

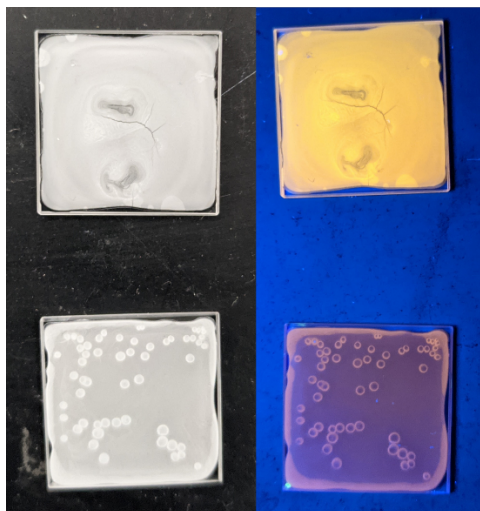


Figure S72: Emission of A in polymer films.

13. References:

1. Lenher *et al. J. Am. Chem. Soc.* **1925**, 47, 3, 772-774.
2. Hattne *et al. Acta Crystallogr. A Found. Adv.* **2015**, 71, 353-360.
3. Nannenga *et al. Nat. Methods* **2014**, 11, 927-930.
4. Kabsch *Acta Crystallogr. D Biol. Crystallogr.* **2010**, 66, 125-132.
5. Sheldrick *et al. Acta Crystallogr. A Found. Adv.* **2015**, 71, 3-8.
6. Hubschle *et al. J. Appl. Crystallogr.* **2011**, 44, 1281-1284.
7. Peng *Micron* **1999**, 30, 625-648.
8. Fairley *et al. Applied Surface Science Advances* **2021**
doi.org/10.1016/j.apsadv.2021.100112
9. Mills *et al. Inorg. Chem.* **2021**, 60, 24, 19165-19174.
10. Plešek *et al. Coll. Czech. Chem. Commun.* **1981**, 46, 687-692.
11. Zakharkin *et al. Phosphorus and Sulfur* **1984**, 20, 357-370.
12. Polgar *et al. Inorg. Chem.* **2019**, 58, 5, 3338-3348.
13. Mils *et al. J. Am. Chem. Soc.* **2020**, 142, 4586-4591.